Title
Modeling Pulsed Laser Melting of Embedded Nanoparticles

Author
Sawyer, Carolyn Anne

Publication Date
2013

Peer reviewed|Thesis/dissertation

Modeling Pulsed Laser Melting of Embedded Nanoparticles

by

Carolyn Anne Sawyer

A dissertation submitted in partial satisfaction of the
requirements for the degree of
Doctor of Philosophy

in

Engineering – Materials Science and Engineering

in the

Graduate Division

of the

University of California, Berkeley

Committee in charge:

Professor Daryl C. Chrzan, Chair
Professor Eugene E. Haller
Professor Tarek I. Zohdi

Spring 2013

Modeling Pulsed Laser Melting of Embedded Nanoparticles

Abstract

Modeling Pulsed Laser Melting of Embedded Nanoparticles

by

Carolyn Anne Sawyer

Doctor of Philosophy in Engineering – Materials Science and Engineering

University of California, Berkeley

Professor Daryl C. Chrzan, Chair

A model of pulsed laser melting of embedded nanoparticles is introduced. Pulsed laser melting (PLM) is commonly used to achieve a fast quench rate in nanoparticles; this model enables a better understanding of the influence of PLM on the size distribution of nanoparticles, which is crucial for studying or using their size-dependent properties. The model includes laser absorption according to the Mie theory, a full heat transport model, and rate equations for nucleation, growth, coarsening, and melting and freezing of nanoparticles embedded in a transparent matrix. The effects of varying the laser parameters and sample properties are studied, as well as combining PLM and rapid thermal annealing (RTA) processing steps on the same sample. A general theory for achieving narrow size distributions of nanoparticles is presented, and widths as narrow as 12% are achieved using PLM and RTA.

Contents

List of Figures

Acknowledgments

This work was supported by the Director, Office of Science, Office of Basic Energy Sciences, Materials Sciences and Engineering Division, of the U.S. Department of Energy under Contract No. DE-AC02-05CH11231.

I would like to thank a number of colleagues and collaborators at U. C. Berkeley and Lawrence Berkeley Lab. First, thanks to my experimental collaborators led by professor E. E. Haller: staff scientist J. W. Ager III and graduate students J. Guzman and K. C. Bustillo; their work and insights were invaluable to my project. Second, I would like to thank my theoretical collaborators M. P. Sherburne, C. N. Boswell-Koller, J. P. Mastandrea, and J. Chua, for productive conversations and commiseration, and especially to M. P. Sherburne for helping me navigate graduate school and fix computers. I gratefully acknowledge the work of C. W. Yuan, whose codebase I inherited and learned a great deal from. I'd also like to thank my other group-mates, Y. Hanlumyang, S. Chen, Y. Zhou, and I. Winter for insightful questions and suggestions. Lastly, I owe a debt of gratitude to professor D. C. Chrzan for his unflagging support and encouragement, for teaching me a great deal, and for guiding me in becoming a better scientist.

Chapter 1

Introduction

1.1 Motivation

Size effects and distributions

Nanoscale and nanostructured materials offer a wide range of novel properties, including electronic and optical properties. For example, there is a quantum size effect on the bandgap: the gap widens significantly as the particle size drops below a few nanometers[1]. This in turn affects the optical spectra, and offers the possibility of tuning the optical spectrum by changing the nanoparticle size. There are also size effects that are not quantum in nature; for example, the surface plasmon of a spherical particle occurs at a frequency that depends on the size. This effect comes out of the purely-classical Maxwell equations, in the form of the Mie theory[2]. These effects interact, as the particle's dielectric function is modified by the quantum size effect, and the plasmon frequency depends on the dielectric function as well as the size.

Nanoparticles also exhibit unique thermodynamic and kinetic behavior, as the properties of the surface have a greater effect on the overall stability of the particle because a greater fraction of the atoms are at the surface as the size decreases. For example, the equilibrium melting point is usually depressed due to the difference in surface energy between the solid and liquid phases[3]. Both supercooling and superheating of embedded nanoparticles have been observed experimentally; this hysteresis arises due to changes in the second-phase nucleation rate due to the interface energies[4]. Embedding nanoparticles in a matrix allows the interface energies to be varied by changing the matrix material, allowing for better engineering of interface energy effects than with free particles alone. Tailoring the melting point and melting hysteresis of nanoparticles could lead to new, more efficient thermal transport and storage systems.

Studying the size-dependent properties of nanoparticles is complicated by the fact that many processes to fabricate nanoparticles result in a broad distribution of sizes within a sample. The size distribution is the number density of particles as a function of the particle radius; the distribution width is typically reported in terms of the full width at half maxi-

mum of this distribution, scaled by the average radius. For instance, embedded nanoparticles created by ion-beam synthesis (IBS) may have a size distribution between 80% and 100% wide[5]. The coarsening distribution, obtained for instance by annealing embedded particles, is around 50% wide[6, 7]. The narrowest size distributions currently obtainable are around 9% wide[8, 9], obtained using a wet chemical method known as size focusing[10]; this method results in free-standing particles or particles suspended in solution, so while beating this record is desirable, just matching it in an embedded system would also be a significant accomplishment. Wide distributions make studying size-dependent properties difficult because most optical, electronic and calorimetric measurement techniques sample more than one nanoparticle at a time, meaning the size-dependent response will be convoluted with the size distribution. Narrow size distributions would also be necessary to utilize size-dependent properties for various applications.

Pulsed Laser Melting

Also known as excimer laser annealing or pulsed laser annealing, pulsed laser melting (PLM) is a widely-used technique for both thin films and nanoparticles. In this process, one or more short (a few picoseconds to a few tens of nanoseconds), high-energy (a few to a few hundred mJ per cm^2) laser pulses are directed at the sample. The primary effect is very rapid heating, followed by very rapid cooling when the pulse ends; this may result in melting, ablation, or annealing depending on the sample and the laser power used.

PLM has been shown to produce a fast enough cooling rate to mix and amorphize alloy nanoparticles[11]. PLM and a slower annealing step (rapid thermal annealing, RTA) may be used to switch binary alloy nanoparticles between a mixed and a phase-segregated state, with possible applications in phase-change memory[11, 12, 13]. Phase-change memory devices, in general, use nanostructures which can be switched between two phases with different optical or electronic properties; bits are written by switching to one phase and erased by switching back, and the data is read by probing a phase-dependent property. Ideally, materials systems for phase-change memory use should have a fairly low-energy switch mechanism that can be embedded safely and cost-effectively in consumer electronics, good stability of the metastable phase for long periods without energy input, and stability of the device to a large number of write/erase cycles. Germanium-gold nanoparticles embedded in glass have been shown to withstand ten PLM-RTA cycles without noticeable degradation in the particles, judging by the Raman signal[13]. However, laser irradiation of nanoparticles has also been shown to produce size[14, 15] and shape[15, 16] changes in nanoparticles, which could degrade the properties of a phase-change device over a larger number of cycles.

A quantitative understanding of the effect of PLM on the size distribution of nanoparticles is needed either to design this type of phase-change material or to take advantage of the size-changing effects of PLM to narrow the size distribution. Because PLM involves a short (*e.g.* 30 ns) laser pulse and nanoscale particles, observing the process *in situ* is experimentally difficult. A predictive model of the effect of PLM on the size distribution of nanoparticles would help to develop this understanding and guide future experiments. Ideally, one set of

laser parameters would be found that produces fully reversible size changes that would not degrade phase-change memory devices, and another set of laser parameters could be found that exploits the size changing capability to produce narrow distributions.

1.2 Prior Work

Prior models of pulsed laser melting have largely focused on thin metallic or semiconductor films[17, 18, 19, 20], rather than on discrete particles. PLM is commonly used for dopant diffusion and removing ion implantation damage from semiconductor films[19]. PLM on metallic films may lead to dewetting and formation of islands[20], or to vaporization of the film at higher energies[17]. The relevant processes therefore are absorption of the laser and conversion of the energy to heat, diffusion of heat and dopants through a thin film, motion of a melt front, dewetting, and loss of the film to vaporization. The absorption and diffusion problems are essentially one-dimensional along the thickness of the film. However, the reflectivity change on melting and the temperature-dependent transport properties make the process non-trivial to model[17, 18, 19].

In the case of embedded nanoparticles, the laser absorption is more complicated; depending on the laser wavelength and the particle and matrix materials, the laser may be absorbed by the particles, the matrix, or both. The heat transport problem is in principle three-dimensional. Instead of a melt front, the number of solid and liquid particles, and the effect of their sizes on melting, is of interest. Diffusion of dopants is no longer one-dimensional, as clusters exchange atoms via dissolution in the matrix. Overall, the problem has higher dimensionality and requires a different computational approach.

A mean-field rate equations approach has been used successfully to model ion beam synthesis of nanoparticles[5, 21, 22], a related problem in that both concern nanoparticles embedded in a low-solubility matrix. This model considers diffusion of dissolved atoms, attachment to and detachment from clusters, and other processes relevant to ion implantation, specifically the addition of implanted ions and fragmentation of particles by impinging ions. Its results include a prediction for the size distribution of nanoparticles created by ion beam synthesis that matches experimental results[22] for several nanoparticle materials. Thus it serves as a reasonable starting point for a model of the effect of PLM on the size distribution of embedded nanoparticles.

1.3 Organization of This Work

This work presents a model of PLM of embedded nanoparticles. It is built on a self-consistent mean-field rate equations framework, and includes three main effects. One is the absorption of the laser, which must be treated by the Mie solution of Maxwell's equations due to the small size of the particles, and the subsequent diffusion of heat. The second main effect is the size evolution of the particles as atoms detach and dissolve into the matrix,

diffuse, and then re-attach to other clusters. The last main effect is melting; the melting rate of a particle is size-dependent, and the phase of a particle affects the detachment and attachment rates by which it grows or shrinks. These three problems, and how they are synthesized into one coherent model, are discussed in Chapter 2. Also discussed are slight modifications to this model or the earlier ion beam synthesis model to simulate rapid thermal annealing and the size focusing technique.

Chapter 3 presents some results of the model, including the results of varying the input parameters of the model and testing the suitability of the system for phase-change memory devices. Chapter 4 concerns a recipe for using PLM and RTA to narrow the size distribution of embedded nanoparticles, and discusses the relation of this method to a more general theory of size distribution narrowing. Conclusions are presented in Chapter 5.

Chapter 2

Model of Pulsed Laser Melting

During pulsed laser melting of embedded nanoparticles, several processes occur simultaneously. The elevated temperature leads to diffusion of atoms dissolved in the matrix, which facilitates nucleation, growth and coarsening of the particles. The kinetics of particle melting depend on the particle size, and in turn whether the particles are molten or solid has an effect on the coarsening. These linked processes are captured in the model by a rate equations approach, in which the rates of melting, growth, and dissolution of particles are calculated to create a set of simultaneous differential equations.

The model framework used, which follows the models developed by Yuan and Yi[5, 6, 7, 21, 22], considers the particle size as the most important property; the positions of the particles are not tracked at all. The mean number density of each size of particle is tracked, *e.g.* $\langle n_5 \rangle$ is the number of particles of five atoms, per unit volume, averaged over a large total volume. The framework will be discussed more in sections 2.4 and 2.6.

2.1 Experimental System to be Modeled

The target system of this model is germanium nanoparticles embedded in silica, similar to that studied experimentally by Xu and Sharp *et al.*[4, 23, 24]. The experimental system is grown by ion implantation of Ge ions into clean silica. The volume fraction of Ge is on the order of 6 atomic percent, with most of the germanium being precipitated into nanometer-scale clusters with a cluster size distribution characteristic of the ion beam synthesis process[5, 21, 22]. The implantation process causes the particles to be concentrated at a particular depth in the sample, leading to a multi-layer structure with layers of unimplanted silica sandwiching the implanted layer, and a silicon substrate below (Figure 2.1). The implanted layer is roughly 100nm thick, and the model neglects the variation of the germanium concentration with depth, assuming instead that the particles are uniformly distributed within this region.

A related experimental system which bears mentioning is that studied by Shin and Guzman *et al.*[11, 12, 13]. This system simply replaces the germanium particles with binary eutectic alloy particles, such as Ge-Au or Ge-Sn. Although the model does not allow for

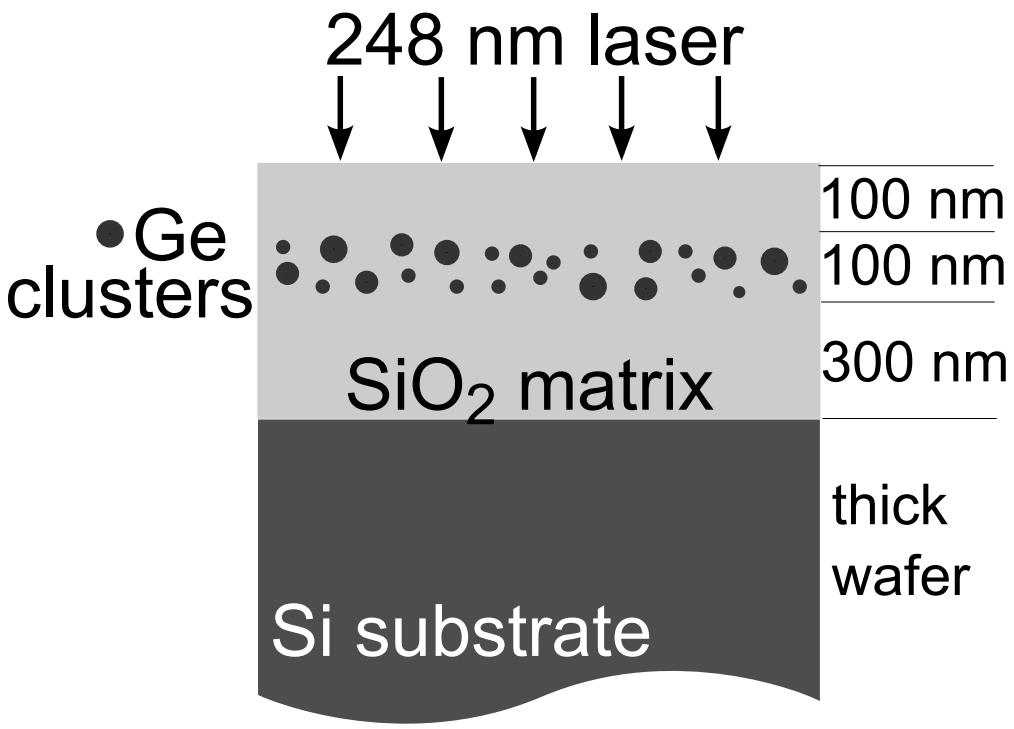

Figure 2.1: Diagram of the sample geometry for the PLM model. The particles occupy an implanted layer 100 nm thick, sandwiched between two layers of silica. Below this sandwich is a thick layer of silicon, and above it is air; the laser light comes in from this side.

these complicated particles, some of the results are generally applicable to this system.

The procedure being modeled is a pulsed laser melting experiment, in which a very high-power laser pulse strikes the sample, causing melting. In this case the laser is assumed to have a 248-nm wavelength (5 eV), a pulse length of approximately 30ns, and to deposit a total 0.3 J/cm^2 fluence; these properties correspond to the KrF excimer laser used in ref.[13].

2.2 Laser Absorption

The full electromagnetic solution to the problem of a plane wave of light striking an isolated, spherical particle was solved by Gustav Mie[25] in 1908. Mie's solution takes the dielectric function of the particle and the material it is embedded in, the size of the particle, and the wavelength of the incoming light, and through a direct solution of the Maxwell equations gives the scattering and absorption cross-sections of the particle. The individual cross-sections can then be used to generate an effective absorption coefficient for the implanted layer, which in turn can be used to calculate the total light energy absorbed by the particles. Assuming that the energy absorbed is converted entirely to heat, this gives a heat power input to the simulation.

The Mie Theory

The Mie theory begins with the Maxwell equations. The geometry used is a spherical particle embedded in a non-absorbing, infinite medium with an incident plane wave. The solution is broken into three parts: the electric and magnetic fields inside the particle, the incident plane wave, and the scattered wave, which superposes with the incoming wave outside the particle. All three parts are expanded in terms of the spherical Bessel functions and Legendre polynomials, which give a complete basis[2]. The incident wave is known, and the other two parts are solved using boundary conditions at the particle surface,

$$(\mathbf{E}_{inc} + \mathbf{E}_{sca}) \times \mathbf{n}|_{r=R} = \mathbf{E}_{part} \times \mathbf{n}|_{r=R} \tag{2.1}$$

$$(\mathbf{H}_{inc} + \mathbf{H}_{sca}) \times \mathbf{n}|_{r=R} = \mathbf{H}_{part} \times \mathbf{n}|_{r=R} \tag{2.2}$$

where $\mathbf{E}$ and $\mathbf{H}$ are the electric field and auxiliary magnetic field; the subscripts refer to whether the field is in the incoming wave, the scattered wave, or inside the particle; $\mathbf{n}$ is the unit normal to the particle surface; and R is the particle radius[2]. The Poynting vector $\mathbf{E} \times \mathbf{H}$ for each part of the solution gives the energy flux into the particle and the energy flux being scattered; integrating this over the surface of the particle gives the cross-sections.

While the full solution is quite involved, a simplification can be made in the case that $2\pi R|\sqrt{\varepsilon}| \ll \lambda$, with ε the complex dielectric function of the nanoparticle material, and λ the wavelength of the incoming light. In this case, which holds for the system considered here, the cross-sections for a particular size of nanoparticle are given by[26]

$$\sigma_{absorption} = 8\pi^2 R^3 \frac{\Re(\sqrt{\varepsilon_m})}{\lambda} \Im\left(\frac{\varepsilon - \varepsilon_m}{\varepsilon + 2\varepsilon_m}\right) \tag{2.3}$$

$$\sigma_{scattering} = \frac{128\pi^5}{3} R^6 \left(\frac{\Re(\sqrt{\varepsilon_m})}{\lambda}\right)^4 \left|\frac{\varepsilon - \varepsilon_m}{\varepsilon + 2\varepsilon_m}\right|^2 \tag{2.4}$$

with ε_m the dielectric function of the matrix material; $\Re$ and $\Im$ are the real and imaginary part functions respectively. It should be noted that the Mie solution assumes that ε_m is wholly real; this is equivalent to the matrix being non-absorbing.

Dielectric Functions

The dielectric functions, along with the particle size, are the only parameters to enter the Mie solution. However, the dielectric function of a material is complex, and both parts may vary with the wavelength of the light, the temperature, and the size of the particles. Fortunately, the dielectric function of germanium is fairly well-documented; Viña *et al.*[27] gives the function of solid germanium over a wide range of temperatures at the wavelength used here. Liquid germanium is less well documented; Jellison *et al.*[28] gives the reflectivity of the liquid close to the melting transition as well as an estimate of the absorption coefficient, from which a dielectric function can be calculated. For this model, for lack of better data,

these estimates are used for all temperatures of the liquid; the model would certainly benefit from better data. Significant superheating of the solid is observed before melting (see section 2.5); the dielectric function for the solid is simply extrapolated to this temperature regime.

There is substantial debate concerning the quantum size effect in germanium[29, 30, 31, 32, 33], which would affect the dielectric function as the particles approach nanometer sizes. Blueshifts in the absorption spectra are observed, but the magnitude and size-dependence of these shifts are not agreed upon. The present work follows the claims of Uhrenfeldt *et al.*[26], who show that many of the reported shifts may be explained by the Mie theory without invoking any quantum size effects; the difference in spectra between spherical particles and an equivalent-volume flat layer is significant and often neglected. Whether to include the quantum size effect, and which of several possible versions to use, turns out to have very little effect on the model; the absorption and scattering cross-sections scale as the particle volume and volume squared respectively, so the larger particles (for which the size effect is least pronounced) outweigh the contributions of smaller particles.

Non-interacting Particles

In principle, proximate particles interact with each other, and the Mie theory explicitly does not account for this interaction. For example, light scattered from one particle may strike another particle, with some particular polarization and brightness that varies from point to point. Groups of particles may have collective optical properties that are very different from the individual particles' properties. A generalized multiparticle Mie[34] theory has been developed to account for these interactions. However, a far simpler approximation exists in the case that the volume fraction of particles is small or their scattering cross-sections are small compared to absorption and transmission. In these limits, the latter of which applies to the Ge particles used in this model, the particles can be considered as non-interacting, and the effective absorption coefficient of the particle/matrix composite is simply

$$\alpha_{absorption} = \sum_j \langle n_j \rangle \sigma_{j,absorption}. \tag{2.5}$$

The scattering coefficient is, similarly,

$$\alpha_{scattering} = \sum_j \langle n_j \rangle \sigma_{j,scattering}. \tag{2.6}$$

and the overall attenuation coefficient is $\alpha = \alpha_{absorption} + \alpha_{scattering}$.

The non-interacting particle assumption also makes it easy to distribute the total heat absorbed amongst the particles; each particle gets a portion of the total absorbed heat proportional to its absorption cross-section. Because the locations of the particles within the layer are not tracked, the intensity of the incoming light at their locations is not known, so using the cross-section directly is not possible. Given an intensity absorbed by the composite layer I_{abs}, the mean volumetric power to the implanted layer is I_{abs}/h with h the layer

thickness. This must equal the sum of the number density of particles times the power absorbed by each particle P_j,

$$\frac{1}{h} I_{abs} = \sum_j \langle n_j \rangle P_j. \tag{2.7}$$

With P_j proportional to $\sigma_{j,absorption}$, and using equation 2.5, this gives

$$P_{j,vol} = \frac{\sigma_{j,abs}}{V} \frac{I_{abs}}{h\alpha} \tag{2.8}$$

with V the volume of the particle, $V = j\Omega$ with Ω the atomic volume.

Macroscale Optics

Because the composite layer is embedded in a multi-layer sample (Figure 2.1), there is an additional larger-scale optics problem to solve; namely, the model must account for light reflected by the top surface of the silica, as well as reflection and absorption from the silicon substrate. The total absorbed intensity is

$$I_{abs} = I_0(1 - R_{air-SiO_2})(1 + \exp(-h\alpha)R_{Si-SiO_2})(1 - \exp(-h\alpha)) \left(\frac{\alpha_{absorption}}{\alpha}\right) \tag{2.9}$$

where I_0 is the intensity from the laser, $R_{air-SiO_2}$ and R_{Si-SiO_2} are reflectances at the air-silica and silica-silicon boundaries; h is the layer thickness and $\exp(-h\alpha)$ the transmission through the implanted layer, and the final term accounts for the fraction of the light that is scattered rather than absorbed. Because the scattering cross-sections for this system are very small, and the air-silica reflectance only a few percent, multiple reflections between the layers are neglected.

A non-trivial amount of light reaches the silicon and is absorbed there, where it provides an additional heat power term. The intensity reaching a depth x from the silicon surface is

$$I_{Si} = I_0(1 - R_{air-SiO_2}) \exp(-h\alpha)(1 - R_{Si-SiO_2}) \exp(-x\alpha_{Si}) \tag{2.10}$$

where α_{Si} is the attenuation coefficient in the silicon; a fraction α_{Si} of this light is absorbed.

2.3 Heat Transport

From the laser absorption considerations given above, there is a set of spherical particles acting as heat sources, embedded in an unpowered matrix. This composite exists in a layer within a multilayer sample. The heat transport problem is thus broken into two parts: first the individual particles are treated in relation to the matrix, and then the heat transport out of the composite layer is calculated.

Particles

Each particle can be treated as a sphere embedded in an infinite matrix. Andrä *et al.*[35] give the temperature rise as a function of time within a uniformly powered sphere, embedded in an unpowered matrix, as

$$\Delta T(r \leq R, t) = \frac{PR^2}{3\lambda_2}\left[1 + \frac{q_\lambda}{2}\left(1 - \frac{r^2}{R^2}\right) + \frac{6}{\pi} q_\lambda^{3/2} q^{1/2} \frac{R}{r} \int_0^\infty f(z,r,t) g(z,r) dz\right] \tag{2.11}$$

with R the radius of the particle, P the volumetric power input, and the abbreviations

$$q_\lambda = \frac{\lambda_2}{\lambda_1} \qquad q = \frac{\rho_2 c_2}{\rho_1 c_1} \qquad g(z,r) = \sin\frac{rz}{R} \tag{2.12}$$

$$f(z,r,t) = z^{-2} \exp\left(-\frac{\lambda_1 t z^2}{\rho_1 c_1 R^2}\right)\left(\frac{z\cos z - \sin z}{((q_\lambda - 1)\sin z + z\cos z)^2 + q_\lambda q (z \sin z)^2}\right). \tag{2.13}$$

The thermal conductivity, density, and heat capacity are λ, ρ and c, where subscript 1 is the particle (germanium) and subscript 2 the matrix (silica). The temperature within the particle is given by ΔT plus some starting temperature T_0. Integrating $\rho_1 c_1 \Delta T$ over the particle volume gives the total amount of heat retained in the particle; the rest of the heat input is transferred to the matrix.

Because the positions of the particles are not tracked, the full heat transport problem, which may for instance produce hot spots between adjacent particles and cool regions where the particles are farther apart, cannot be calculated. Instead, the heat power that is not retained in the particles is applied uniformly to the entire composite layer. This, together with the heat transport between layers described below, gives the baseline temperature for the composite; points within a particle are taken to have a total temperature $T = T_0 + T_{layer}(t) + \Delta T(r,t)$. This method is somewhat ad hoc; however, it maintains conservation of energy and presents a reasonable picture of heat transport without too much computational expense. It is also consistent with the mean-field approach used in section 2.4 for mass transport.

In principle, the heat transport properties (λ, ρ, and c) depend on temperature. However, this effect is relatively small, and is neglected to save computational expense; the solution ΔT depends linearly on the power P, so can be pre-calculated as a function of particle size. If this effect becomes important, the corresponding steady-state solution

$$\Delta T(r \leq R) = \frac{PR^2}{3\lambda_2}\left[1 + \frac{q_\lambda}{2}\left(1 - \frac{r^2}{R^2}\right)\right] \tag{2.14}$$

can be used instead of equation 2.11; for particles on the order of a hundred atoms the time-dependent and steady-state solutions agree within 5% after one tenth of a nanosecond, the time step used in the model. This solution has the advantage of being much easier to calculate as it does not have the z-integral that appears in the time-dependent solution.

Layers

The sample overall can be treated as a semi-infinite layer of air, a layer of unimplanted silica, the composite layer which is receiving a uniform heat power from the particles embedded in it, another layer of silica, and finally a semi-infinite layer of silicon substrate, whose surface is absorbing some leftover light and converting it to heat. Within the solid layers, heat conduction dominates, but radiation may play an important role at the air interface as the silica heats up. The layered sample symmetry allowing a 1-dimensional model, the multiple mechanisms of heat transfer, and the multiple localized heat sources are conducive to a finite difference heat transfer model. In the finite difference framework, the heat equation becomes

$$\Delta T(x) = \frac{\Delta t}{\Delta x}\left(\frac{a(x+\frac{\Delta x}{2})}{\Delta x}(T(x+\Delta x)-T(x)) - \frac{a(x-\frac{\Delta x}{2})}{\Delta x}(T(x)-T(x-\Delta x))\right) + \Phi(x)\Delta t \tag{2.15}$$

where $a(x) = \frac{\lambda}{c\rho}$ is the combined thermal properties of the material at location x and $\Phi(x)$ is any volumetric power input or output modified by $\frac{1}{c\rho}$. The step Δx should be sufficiently small to resolve the different layers; $\Delta x = 5$ nm was chosen, placing 20 sample points in the implanted layer. Stability concerns then limit the size of Δt; 10^{-13} seconds was chosen.

There are three regions where a heat power is assumed to be in effect; the implanted layer has heat leaving the particles, the silicon surface is absorbing the laser that makes it through the implanted layer, and blackbody radiation from the silica surface into the adjacent air cannot be neglected at very high temperatures. In the implanted layer,

$$\Phi(x_{implanted}) = \frac{1}{c\rho}\sum_j \langle n_j \rangle \left(PV_j - \int_{V_j} c_1\rho_1 \frac{\Delta T_j(r)}{\Delta t} dV\right) \tag{2.16}$$

where c and ρ are the properties of the implanted layer, which is a composite of the matrix and nanoparticles; because the volume fraction of the nanoparticles here is fairly low, the properties of the silica matrix were used. At the surface of the silicon substrate,

$$\Phi(x_{silicon}) = \frac{1}{c\rho}\alpha_{Si,absorption} I_{Si}(x) \tag{2.17}$$

where $I_{Si}(x)$ is the intensity reaching a depth x as given by equation 2.10. The radiative heat loss at the surface is treated, for simplicity's sake, as blackbody radiation following the Stefan-Boltzmann law $P = \sigma A T^4$. Here, σ is the Stefan-Boltzmann constant and A is the area radiating. In the finite difference model, this is treated as a volumetric power term in the first silica element at the surface,

$$\Phi(x_{surface}) = \frac{\sigma T(x)^4}{c_2\rho_2\Delta x}. \tag{2.18}$$

It should be noted that this is a fairly crude approximation, but treating the silica as a blackbody allows reasonable bookkeeping of the temperature without including the full wavelength-dependent dielectric function.

The finite difference model has the initial condition that $T = T_0$, where T_0 is room temperature, and the boundary conditions that $T(x = 0) = T(x_{max}) = T_0$, where $x = 0$ is a thick layer of air away from the silica surface and x_{max} is deep into the silicon substrate. The thicknesses of these layers were chosen such that increasing the thickness had no discernible impact on the simulation temperature; this corresponds to $T \to T_0$ as $x \to \pm\infty$. At the boundaries between different layers, thermal resistance is neglected, leading to the additional condition that the temperature is equal as a boundary is approached from either side; the x points are placed such that the temperature at layer boundaries is explicitly tracked. The solution method uses central differences in space and explicit (forward) Euler steps in time.

2.4 Coarsening

Thus far, given a distribution of particle sizes in the matrix and a laser power, the model predicts the temperatures reached over time. However, insight into the evolution of the particle size distribution is the main goal of this work, either to find processing routes to narrow the distribution or to evaluate the lifetime of phase-change memory systems. The particle size distribution may change as particles nucleate, grow and coarsen; these processes are mediated by atoms dissolving from the surface of particles, diffusing through the matrix, and attaching to other clusters (or attaching to other dissolved atoms to nucleate new clusters). The rates at which particles grow or shrink depend on temperature and on the size and properties of the particles. The following derivation follows the work of Yi (refs. [6, 7]) and Yuan (refs. [5, 21, 22]), but accounts for the effects of temperature, especially the temperature gradient surrounding the particles.

Two main rates are identified for each size of particle: the mean time τ_j between desorption events, when an atom leaves the particle, and the capture rate $D\sigma_j\langle n_1\rangle$, which represents the rate at which dissolved atoms at a mean concentration $\langle n_1\rangle$ are absorbed by the particle. These two rates include the effects of diffusion of dissolved atoms. With these two rates for each particle, a set of rate equations can be constructed. The rate equations for the mean concentration of dissolved atoms is:

$$\frac{d\langle n_1\rangle}{dt} = -2D\sigma_1\langle n_1\rangle^2 - D\sum_{j>1}\sigma_j\langle n_1\rangle\langle n_j\rangle + 2\frac{\langle n_2\rangle}{\tau_2} + \sum_{j>2}\frac{\langle n_j\rangle}{\tau_j} \tag{2.19}$$

where the first term covers nucleation of 2-clusters, the second term covers absorption of dissolved atoms by all larger particles, the third term covers dissolution of a 2-cluster into two atoms, and the last term covers desorption of atoms by all larger clusters. The rate equations for all other particles are:

$$\frac{d\langle n_j\rangle}{dt} = D\sigma_{j-1}\langle n_1\rangle\langle n_{j-1}\rangle - D\sigma_j\langle n_1\rangle\langle n_j\rangle - \frac{\langle n_j\rangle}{\tau_j} + \frac{\langle n_{j+1}\rangle}{\tau_{j+1}}. \tag{2.20}$$

where j is the size of the particle in atoms. The first term covers an increase in the number of j-particles when a smaller $(j-1)$-particle absorbs an atom and becomes a j-particle. The

second term covers loss of j-particles by growing into $(j+1)$ particles. The third and fourth terms cover dissolution and shrinking, as j-particles become $(j-1)$-particles and $(j+1)$-particles become j-particles. The rate equations are coupled, and there is one equation for each size of particle in the system; this leads to a large system of simultaneous differential equations.

The rates $1/\tau$ and σ can be calculated by a self-consistent mean-field approach. Each particle size is considered individually, while all other particles are treated as sources and sinks of dissolved atoms which are smeared uniformly in space. The dissolved atom concentration is allowed to vary in space, $n_1(\vec{r},t)$, under the self-consistency condition that at infinite distance from a particle, the concentration approaches its mean value,

$$\lim_{r\to\infty} n_1(\vec{r},t) = \langle n_1 \rangle. \tag{2.21}$$

Under these conditions, the diffusion-reaction equation that governs $n_1(\vec{r},t)$ is

$$\frac{\partial n_1(\vec{r},t)}{\partial t} = \nabla \cdot (D\nabla n_1(\vec{r},t)) + \mathcal{J} - D\xi^{-2} n_1(\vec{r},t) \tag{2.22}$$

where $\mathcal{J}$ is the total source term and $D\xi^{-2}n_1(\vec{r},t)$ the sink term. The equivalent equation for the mean concentration of dissolved atoms is

$$\frac{d\langle n_1 \rangle}{dt} = \mathcal{J} - D\xi^{-2}\langle n_1 \rangle. \tag{2.23}$$

Comparing this equation to equation 2.19, the identifications

$$\mathcal{J} = 2\frac{\langle n_2 \rangle}{\tau_2} + \sum_{j>2} \frac{\langle n_j \rangle}{\tau_j} \tag{2.24}$$

$$\xi^{-2} = 2\sigma_1 \langle n_1 \rangle + \sum_{j>1} \sigma_j \langle n_j \rangle \tag{2.25}$$

are made. Defining $\eta \equiv n_1(\vec{r},t) - \langle n_1 \rangle$ and combining equations 2.22 and 2.23,

$$\frac{\partial \eta}{\partial t} = \nabla \cdot (D\nabla\eta) - D\xi^{-2}\eta. \tag{2.26}$$

It is assumed that $\frac{\partial \eta}{\partial t}$ is very small or zero for all r; in other words, the rate of change of $n_1(r)$ does not vary much from the rate of change of the average value $\langle n_1 \rangle$[6]. Thus equation 2.26 becomes

$$0 = \nabla \cdot (D\nabla\eta) - D\xi^{-2}\eta. \tag{2.27}$$

The self-consistency equation gives a boundary condition at large r, but a second boundary condition is needed. The flux of dissolved atoms out of a particle is given by

$$J_{s,continuum} \equiv -4\pi (R_s')^2 D \left.\frac{\partial n_1}{\partial r}\right|_{R_s'}. \tag{2.28}$$

where R'_s is an attachment distance, the distance between the particle center and the center of a dissolved atom just before attachment or just after detachment. Another formulation for the flux comes from considering the movements of individual atoms during attachment and detachment; this is given by[6]

$$J_{s,atomistic} = 4\pi R_{s+1}^2 \frac{D}{a} n_\infty e^{(\Gamma/R_{s+1})} - 4\pi (R'_s)^2 \frac{D}{a} n_1(R'_s) \tag{2.29}$$

where a is the average distance between sites a dissolved atom can occupy. The first term is the detachment rate, where n_∞ is the solubility of atoms in the matrix in equilibrium with a flat surface ($R = \infty$) and $\exp(\Gamma/R_{s+1})$ is the modification for spherical particles that comes out of the Gibbs-Thomson relation[6]. The second term is the attachment rate given a concentration n_1 of dissolved atoms at the attachment distance. Equating the two expressions gives a Robin boundary condition at the particle surface,

$$\left.\frac{\partial n_1}{\partial r}\right|_{R'_s} = \frac{1}{a} n_1(R'_s) - \frac{R_{s+1}^2}{(R'_s)^2} \frac{1}{a} n_\infty e^{(\Gamma/R_{s+1})}. \tag{2.30}$$

With these two boundary conditions, equation 2.27 can be solved to find the dissolved atom concentration and the flux everywhere outside the particle.

The flux J also relates to the rates σ and τ that are sought;

$$J_s = \frac{1}{\tau_{s+1}} - D\sigma_s \langle n_1 \rangle. \tag{2.31}$$

Thus, $\sigma_s = \frac{1}{D}\frac{dJ}{d\langle n_1\rangle}$ and $\frac{1}{\tau_{s+1}} = J_s + D\sigma_s\langle n_1\rangle$; the derivative can be estimated by a central-difference formula, where J is calculated twice at values of $\langle n_1\rangle$ slightly above and slightly below the true value, where ε is a small number,

$$\sigma_s \approx \frac{1}{D} \frac{J((1+\varepsilon)\langle n_1\rangle) - J((1-\varepsilon)\langle n_1\rangle)}{2\varepsilon\langle n_1\rangle}. \tag{2.32}$$

Thus, for each particle size, equation 2.27 must be solved twice at different values of the dissolved-atom concentration. The solution then gives $n_1(R'_s)$, the concentration of dissolved atoms at the particle surface, which is substituted into equation 2.29 to find the flux J.

The diffusion constant $D = D_0 \exp(-E_m/kT)$ depends on the temperature, which varies locally as heat is transported out of the particle. The temperature is given a r^{-1} dependence as in the steady-state solution for temperature outside a uniformly-powered sphere. The temperature at the surface of the particle $T_0 + \Delta T$ has already been calculated for the heat transport problem; the diffusion constant as a function of distance from the particle is then

$$D(r) = D_0 \exp\left(\frac{-E_m}{k(T_0 + \Delta T \frac{R}{r})}\right). \tag{2.33}$$

Because D depends on distance from the particle, the simplification $\nabla \cdot (D\nabla\eta) = D\nabla^2\eta$ cannot be made, and the equation is not analytically solvable. Instead, it is solved by a finite difference method using central differences. The self-consistency condition (equation 2.21) as $r \to \infty$ is replaced by $n_1(R_{max}) = \langle n_1 \rangle$, where $R_{max} = 5(R'_s + \xi)$ was found to be sufficiently large to match the analytical solution in the case that D is constant.

One further complication must be resolved: the value ξ, a length scale that comes out of the mean field approximation, depends on the values of σ_s (equation 2.25) and appears in the calculation of σ_s (equation 2.27). This difficulty is resolved simply by guessing a value of ξ^{-2} and iterating calculations of the σ_s values and of ξ^{-2} until the change in ξ^{-2} is sufficiently small (less than 0.1% of ξ^{-2}) between iterations. The guess for each step of the overall simulation is the result of the previous step, and the guess for the first step is a typical value, 0.03 Å^{-2}. Convergence typically takes one to two iterations.

2.5 Melting

Kinetics of Melting

Melting in embedded nanoparticles may be very different from bulk behavior. Suppression of the equilibrium melting point is observed in many nanoparticles[3] and arises due to the increased importance of the surface energy in the total energy of small particles. A thermodynamic analysis, neglecting mass exchange with the matrix, gives

$$\Delta T_m = \frac{3T_m}{LR}(\gamma_{LM} - \gamma_{SM}) \tag{2.34}$$

where T_m is the bulk melting point, L the latent heat, R the radius of the particle, and γ_{LM} and γ_{SM} are the interface energies between the matrix and the liquid or solid particle respectively[4]. The volume change of the particle on melting, and the associated stress, is neglected here. In the case of germanium in silica, no change in the equilibrium melting point is observed, leading to the conclusion that $\gamma_{LM} = \gamma_{SM}$ in this case[4]. Using the model for a different matrix or particle material would require making the slight modification of a size-dependent equilibrium melting point.

In addition to changes to the equilibrium melting point, hysteresis of the melting point has been observed in embedded nanoparticles[4, 36, 37]. This may be explained by a simple kinetic model of heterogeneous nucleation; the particle is considered to be spherically confined and the second phase forms a lens-shaped nucleus on the sphere surface (see figure 2.2). The change of Gibbs free energy to form such a nucleus is

$$\Delta G = VL\frac{\Delta T}{T_m} + A_{SL}\gamma_{SL} \tag{2.35}$$

where V is the lens volume, L is the latent heat, A_{SL} is the area of the solid-liquid interface and γ_{SL} its interface energy. If the interface energies with the matrix differ, there would be

an additional term $\pm A_{SM}(\gamma_{SM} - \gamma_{LM})$ for the area of the nucleus's interface with the matrix. $\frac{\Delta T}{T_m}$ is the overheating or under-cooling, with $\Delta T = T_m - T$ for melting and $\Delta T = T - T_m$ for freezing. The shape of the lens is determined by Young's equation, where the spherical interface with the matrix is considered to be rigid; because the liquid-matrix and solid-matrix interface energies are equal, the angle between the two surfaces of the lens is 90° (see figure 2.2). The two surfaces of the lens are spherical caps, with the same basal radius but different heights and sphere radii. Parametrizing by the angle θ, measured from the center of the lens to the center of the particle and back to the edge of the lens,

$$\begin{aligned} V =& \frac{\pi h_1^2}{3}(3r_1 - h_1) + \frac{\pi h_2^2}{3}(3r_2 - h_2) \\ =& \frac{\pi r_1^3}{3}(1 - \cos\theta)^2(2 + \cos\theta) + \frac{\pi r_1^3}{3}\tan^3\theta(1 - \sin\theta)^2(2 + \sin\theta) \end{aligned} \tag{2.36}$$

where r_1 is the particle radius, $h_1 = r_1(1 - \cos\theta)$ is the height of the cap on the outside of the particle, $r_2 = r_1 \tan\theta$ is the sphere radius of the cap towards the inside of the particle, and $h_2 = r_1(1 - \sin\theta)$ is the height of the inside cap. This trigonometry is only valid, again, if the interface energies with the matrix are equal and the angle between the two cap surfaces is $\pi/2$. Similarly, the area of the inside cap is

$$A_{SL} = 2\pi r_2 h_2 = 2\pi r_1^2 \tan^2\theta(1 - \sin\theta). \tag{2.37}$$

The maximum of equation 2.35 over θ gives the energy barrier to forming a critical nucleus of a second phase in a particle,

$$\Delta G^* = \max_{0 \le \theta \le \pi} V(\theta) L \frac{\Delta T}{T_m} + A_{SL}(\theta)\gamma_{SL}. \tag{2.38}$$

This energy barrier can then be used to calculate a melting or freezing rate for each particle according to Boltzmann statistics,

$$r = \nu N_{surf} \exp\left(\frac{-\Delta G^*}{kT}\right) \tag{2.39}$$

where ν is an attempt frequency for nucleation on the order of 10^{11} attempts per second per atom[4], and N_{surf} is the number of atoms available to initiate heterogeneous nucleation, *i*.e. those within an atom diameter of the particle surface. This rate can be combined straightforwardly with the rates of coarsening discussed above into one rate equation for each size and phase of particle.

It is not clear that the classical nucleation approach is appropriate as the particle size becomes very small, especially for particles of only a few atoms. Additionally, it is unclear what the phase even means for, for example, two bonded atoms embedded in a matrix, since long-range order doesn't exist regardless of the temperature. However, it has shown good results in particles of a few nanometers radius[4]. In smaller particles, the barrier to classical nucleation decreases with decreasing size to be virtually zero for the particles for which phase is ill-defined; phase transformation with a negligible energy barrier is a reasonable first approximation to the behavior of these tiny particles.

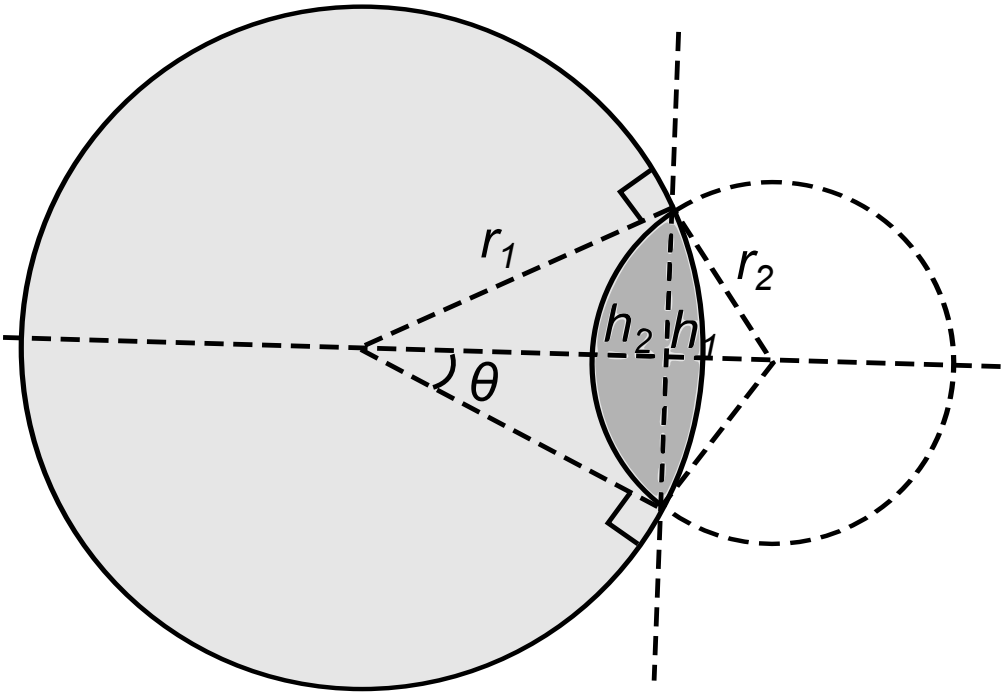

Figure 2.2: Diagram of the geometry of embedded particle melting in the case that the solid and liquid have equal interface energies with the matrix. The two shaded regions are the two different phases within the spherical particle.

Effect on Solubility

The phase of the particle will affect many of the properties that the model uses, including the dielectric function already mentioned; the most important effect is on the solubility around the particle. The solubility is defined as the concentration of dissolved atoms in equilibrium with the particle; this depends on the heat of formation, E_f, of the dissolved atom relative to staying in the particle, according to

$$n = n_0 \exp\left(\frac{-E_f}{kT}\right) \exp\left(\frac{\Gamma}{R}\right)$$

where the latter exponential term is the Gibbs-Thomson effect previously mentioned (see ref. [6]) and n_0 is the density of sites that the dissolved atoms can occupy. The heat of formation depends on the details of how the dissolved atom sits in the matrix, and is generally determined empirically from the solubility relative to a flat surface as a function of temperature. Thermodynamically, the heat of formation is a state function, so its value is independent of the path taken between the atom being part of the particle and being dissolved in the matrix. Therefore, a fictitious path can be invented, where the atom first sublimates from a solid particle into the vacuum, and then is taken from the vacuum into the matrix[38]. The latter portion of this path is independent of the phase of the particle,

so its enthalpy contribution is fixed. In the case of a liquid particle, the heat of sublimation can simply be replaced by the heat of vaporization; thus,

$$E_{f,liquid} = E_{f,solid} - L$$

where L is the heat of fusion, the difference between the heats of sublimation and vaporization. The main result of particle melting, therefore, is a reduction in the heat of formation for solubility, which leads to an increase in the solubility and a Gibbs-Thomson-like driving force for liquid particles to shrink and comparably-sized solid particles to grow.

2.6 Rate Equations Algorithm

Thus far there are several loosely-interconnected parts of the model: laser absorption, heat transport, calculation of rates, and solution of the rate equations. These separate parts must be integrated into a coherent whole. The overall model, similar to the prior work in refs [6, 21], breaks the total simulation time into shorter time steps; on each time step, the laser absorption, sample temperature, and rates for the rate equations are calculated, and the rate equations are solved. A flowchart of the model algorithm is shown in figure 2.3. The main quantity that is tracked through the rate equations is the mean-field number density of particles of each size and phase. The temperatures are tracked through a separate finite-difference scheme. At the start of the simulation, a laser schedule and a starting particle size distribution are set, along with any modifications to the sample geometry and the particle and matrix materials.

Time Splitting Scheme

In the real system, the temperature and the size distribution evolve simultaneously and depend on each other, as the particle size controls how much light is absorbed and the temperature determines the melting and coarsening rates of the particles. However, calculating both simultaneously is very computationally costly. Instead, a splitting scheme is employed whereby the temperature change is calculated based on the size distribution at the beginning of a large time step, and the size distribution change is calculated based on the changed temperature. This type of splitting scheme is, formally, first-order accurate in the large time step.

The PLM simulation, which simulates the 30ns laser pulse plus 70-170 ns cooling time, is broken into 0.1 ns time steps. During each of these time steps, the temperature is updated and then the size distribution is updated. The temperature update is a thousand-step (0.1 ps step) finite difference calculation. The size distribution update consists of first calculating the rates based on the updated temperature and the size distribution at the beginning of the step, and then using those rates to solve a set of rate equations over the 0.1 ns time step. The rate equations are solved by one of MATLAB's built-in solvers, ode15s, using a Jacobian derived from the rate equations.

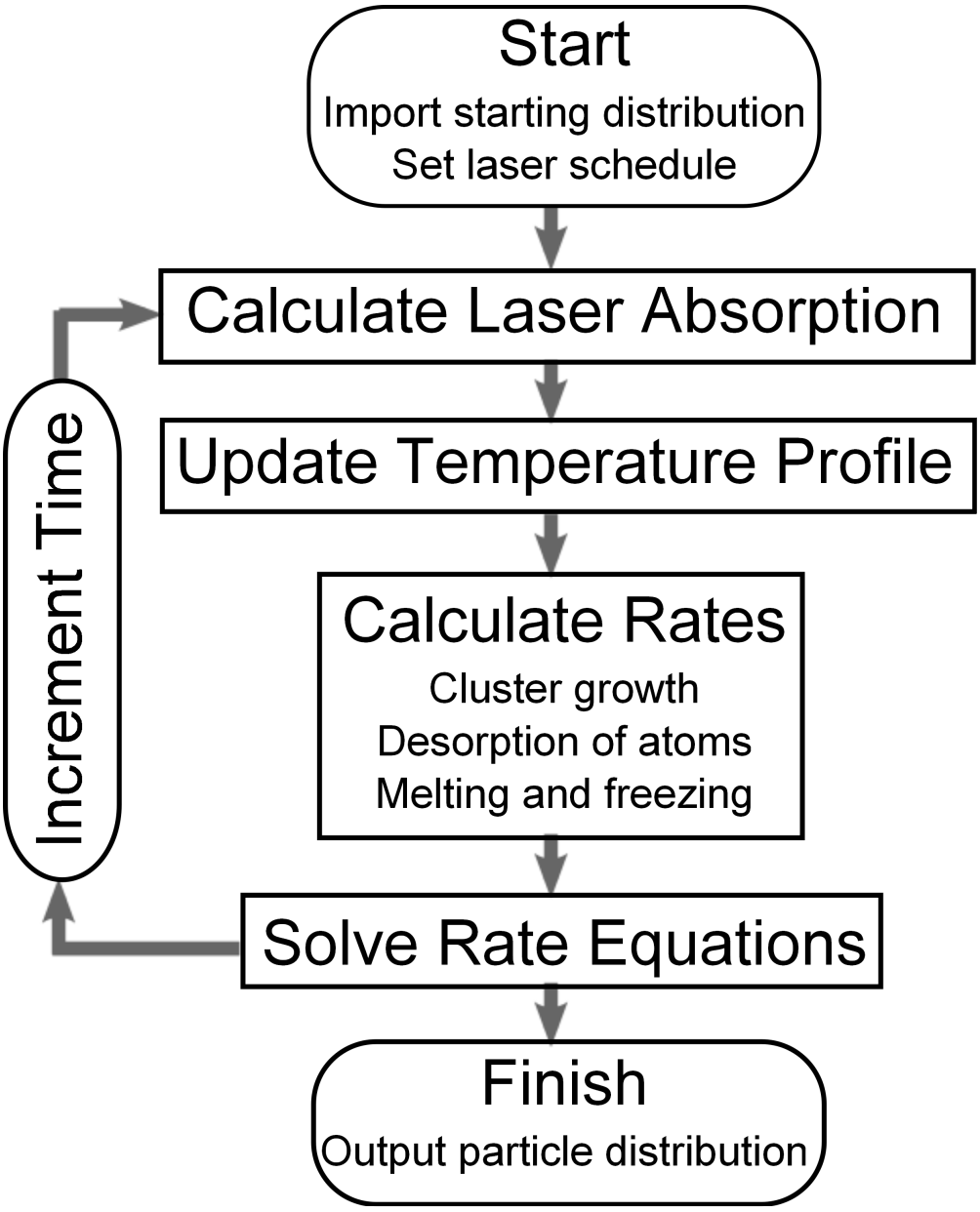

Figure 2.3: Flowchart of the model of PLM.

Because of the melting and freezing transitions, the particle size update and the temperature update interact in one additional way: the latent heat of the transformation. At the end of each time step, the change in the total volume of solid and liquid particles is calculated (by summing the size-weighted numbers of particles). Because individual particles are not tracked, the latent heat can't be applied to the individual particle that melted or froze, so the latent heat is applied to the entire matrix at the start of the next time step. The amount of heat from the laser retained by each particle is small, and the latent heat contribution is small compared to the laser power, so this approximation will not have a large effect on the model results.

Particle Tracking

In the earlier model of ion beam synthesis[21], all particles of the same size had identical atomic absorption and desorption rates, so they were treated the same: instead of tracking every particle individually, the number of particles of the same size was tracked. Once melting is introduced, each phase has different absorption and desorption rates, so it makes sense to split the population of particle sizes into separate populations of solid and liquid particles. The rates are assumed to be independent, *i*.e. a particle of a given size and phase may shrink or grow without changing phase, or may change phase but remain the same size. Thus the solid and liquid populations only interact through size-conserving phase changes and through the shared field of dissolved atoms. Dissolved atoms are treated somewhat specially, in that they are not split into solid and liquid populations, but assigned to all be nominally solid. This, in turn, creates some difficulty in assigning the phase of newly-nucleated two-atom clusters; this is resolved by assigning two-atom clusters to be solid if the matrix temperature is below the equilibrium melting point and to be liquid otherwise.

The governing rate equations, including the melting terms, are

$$\frac{d\langle n_1\rangle}{dt} = -2D\sigma_1\langle n_1\rangle^2 - D\sum_{j>1}(\sigma_{j,s}\langle n_{j,s}\rangle + \sigma_{j,l}\langle n_{j,l}\rangle)\langle n_1\rangle + 2\frac{\langle n_{2,s}\rangle}{\tau_{2,s}} + 2\frac{\langle n_{2,l}\rangle}{\tau_{2,l}} + \sum_{j>2}\left(\frac{\langle n_{j,s}\rangle}{\tau_{j,s}} + \frac{\langle n_{j,s}\rangle}{\tau_{j,s}}\right) \tag{2.40}$$

$$\frac{d\langle n_{2,s}\rangle}{dt} = H(T_m - T)D\sigma_1\langle n_1\rangle^2 - D\sigma_{2,s}\langle n_1\rangle\langle n_{2,s}\rangle - \frac{\langle n_{2,s}\rangle}{\tau_{2,s}} + \frac{\langle n_{3,s}\rangle}{\tau_{3,s}} - r_{2,melt} + r_{2,freeze} \tag{2.41}$$

$$\frac{d\langle n_{2,l}\rangle}{dt} = H(T - T_m)D\sigma_1\langle n_1\rangle^2 - D\sigma_{2,l}\langle n_1\rangle\langle n_{2,l}\rangle - \frac{\langle n_{2,l}\rangle}{\tau_{2,l}} + \frac{\langle n_{3,l}\rangle}{\tau_{3,l}} + r_{2,melt} - r_{2,freeze} \tag{2.42}$$

$$\frac{d\langle n_{j,s}\rangle}{dt} = D\sigma_{j-1,s}\langle n_1\rangle\langle n_{j-1,s}\rangle - D\sigma_{j,s}\langle n_1\rangle\langle n_{j,s}\rangle - \frac{\langle n_{j,s}\rangle}{\tau_{j,s}} + \frac{\langle n_{j+1,s}\rangle}{\tau_{j+1,s}} - r_{j,melt} + r_{j,freeze} \tag{2.43}$$

$$\frac{d\langle n_{j,l}\rangle}{dt} = D\sigma_{j-1,l}\langle n_1\rangle\langle n_{j-1,l}\rangle - D\sigma_{j,l}\langle n_1\rangle\langle n_{j,l}\rangle - \frac{\langle n_{j,l}\rangle}{\tau_{j,l}} + \frac{\langle n_{j+1,l}\rangle}{\tau_{j+1,l}} + r_{j,melt} - r_{j,freeze} \tag{2.44}$$

where $3 \leq j \leq j_{max}$. In other words, there is an equation for each size and phase of particles, with the exception that dissolved atoms are all nominally solid. Newly nucleated 2-clusters are assigned to be liquid or solid based on whether the matrix temperature is above or below the bulk melting point; H is the Heaviside step function. Because the energy barrier for 2-clusters to melt or freeze is negligible, the details of how 2-clusters are assigned to phases aren't important as long as the total nucleation rate is accurate.

One disadvantage of the mean-field approach compared to tracking individual particles is that as the particles become large, a rate equation must be solved for every possible size between single atoms and large clusters, whereas in other approaches calculations may need to be made only for a finite number of individual particles. This is also an advantage, in that the full statistics of the system emerge with only one simulation run, instead of needing multiple runs to accumulate statistics as in kinetic monte carlo. This will be discussed more in the next section, but is relevant to how the particles are tracked in that some care must be taken in choosing the upper bound of the particle sizes j_{max}. In principle, there is a finite probability of forming any arbitrarily large particle in any given time, and thus at the end of the first time step there is a nonzero number density of every size particle. Following the earlier models[6, 21], a cutoff is set where the number density drops below 10^{-15} clusters per cubic angstrom, compared to typical number densities of $10^{-6} - 10^{-4}$ for the highest-density cluster sizes. Whenever the density of the largest-size particle exceeds this cutoff value, an additional thousand larger particle sizes are added to the simulation ($j_{max} := j_{max} + 1000$). The cutoff is lower and the number of sizes to add is much higher than in the earlier model simply because the particles may grow very quickly under the high heating of PLM; these values were determined empirically by checking the amount of mass lost by the simulation when particles of the largest tracked size grew and were dropped out of the simulation.

2.7 Limitations of the PLM Model

Because of the complexity of the real pulsed-laser melting process, many approximations have been made in building the model. These approximations fall into four main categories: using classical treatments at very small sizes and times, ignoring some temperature- or size-dependent properties, ignoring mechanical effects, and sacrificing real-world fidelity to save computational time. The primary justification for all of these approximations will appear if the model is vindicated in experiment; the approximations were made to make the project of modeling PLM feasible and to generate predictions in a reasonable amount of time.

Classical Treatments

The model as it stands is almost entirely classical; the only nod to the quantized nature of matter is that particles are constrained to contain an integer number of atoms. Clusters of two and three atoms are treated as if spherical, following the earlier work[6, 21]. Similarly,

the individual phonons involved in heat transport are ignored in favor of the classical heat transport equation.

For laser absorption, the Mie theory takes into account the sizes of the particles, but is fundamentally a classical approach; the particles are assumed to be perfect spheres with sharp interfaces with the matrix, and the quantum size effect on the dielectric function is ignored. The former may be justified by the good results of the Mie theory in general for extremely small particles[26]. Ignoring the quantum size effect arose out of necessity, as different researchers have published significantly different size effects for germanium[29, 32, 39]. Additionally, the dielectric function depends strongly on the matrix for embedded (or the passivating layer for free-standing) nanocrystals[40, 41]. However, there is some evidence that the approximation will not strongly affect the results of the model. The laser energy is at 5 eV, significantly above the bulk band gap of germanium; for particles of more than about 100 atoms, the absorption at this wavelength is fairly insensitive to the size[42], whereas this would not be true close to the gap. Additionally, the absorption and scattering cross-sections at small sizes are proportional to the volume and the volume squared, respectively, so the effect of small particles on the total light absorbed is small. Measured absorption cross-sections for germanium nanoparticles agree reasonably well with Mie theory simulations using the bulk dielectric function; simulations using the calculated dielectric function of ref. [41] agree equally well, but not better, with experiment[26].

For heat transport, the absorbed laser power is assumed to be instantaneously converted to heat, and the classical heat equation is used. In reality it takes a finite amount of time for optically-excited electrons to thermalize and transfer energy to the matrix. However, these effects take place on the time scale of one to several picoseconds[43], while the model's treatment of the temperature is on the time scale of 0.1ns, the time step for splitting the temperature and particle solution steps (section 2.6). Using the classical treatment is therefore plausible, but not guaranteed to work; the proof of the method is in its results (see section 3.1). Similarly, proof of the reasonability of the coarsening rates comes from the results of the earlier model, which agree well with experiment[5].

Variable Properties

Pulsed-laser melting entails a very large swing in temperature; the temperature-dependence of properties becomes very important. However, the necessary properties are not all well-known over the temperature range, and there are computational-cost reasons to neglect some of them even when literature values exist. The dielectric functions used in the model for the Mie absorption are temperature-dependent, although for the superheated solid these had to be extrapolated from equilibrium values[27, 28], and temperature-dependent values for the liquid were not available. The diffusivity and solubility (n_∞) used are fully temperature-dependent, with both following an Arrhenius relationship.

The thermal properties of the germanium and the silica are kept constant with temperature. The small-scale heat transfer model for transport out of each individual particle is simply proportional to the power, but requires evaluation of a complicated integral for each

relevant particle size. To save computational time, the temperatures at the edges of the particles and the amount of heat retained, scaled by the power, were pre-calculated once for all simulations. The thermal properties used therefore are the room temperature values for the solid phase, regardless of temperature. Better accuracy could be obtained at the expense of computational time by giving these properties their temperature-dependent values.

A related limitation is that despite experimental evidence that PLM amorphizes the germanium particles[13], the properties used for solid germanium throughout the model are those of the crystalline phase. This was necessitated largely because the properties of amorphous germanium are not all available; additionally, the amorphous particles would have needed to be tracked separately from the liquid and crystalline particles, leading to an increase in computational cost.

Pressure

In the experimental system, the nanoparticles formed by ion beam synthesis are under pressures as high as 1.5 GPa[24]; these pressures result from the expansion of germanium during solidification, which is roughly 5%[44]. Similar pressure changes are expected for both the melting and freezing transitions under PLM, and even growing the particles inside a stiff cavity in the silica matrix may introduce pressure. These effects are neglected in the model, and may serve to slow down particle growth and promote or discourage phase transitions. At high temperatures, the silica matrix is expected to relax quickly and relieve the pressure buildup[24], but the freezing transition and the particle growth that take place as the system is cooling would be affected. The justification for using the pressure-free assumptions is that the previous model of ion beam synthesis neglects pressure and still obtains good results[5]. Additionally, the interface energy between solid and liquid germanium that the model uses is derived from experiment using a pressure-free model[4]. Lending additional credence to the pressure-free model, the value found for this interface energy, 0.26 J/m^2, is comparable to the solid-liquid interface energies found for silicon, depending on the method used[45].

Interface Energy and the Prospects for Alloy Particles

The interface energy between solid germanium and silica is estimated to be between 0.7[4] and 1.5[21] J/m^2. The higher the interface energy for a given concentration of dissolved atoms, the larger the critical nucleus size for cluster formation; this in turn leads to a larger average particle size, all other parameters being equal[21]. Because the simulation must calculate rates and solve equations for every size of particle, the computational cost rises quickly with increasing average particle size. To keep computational times feasible, an artificial interface energy of 0.2 or 0.5 J/m^2 is used for many simulations. The effect of changing the interface energy on the results will be discussed in section 3.2.

One of the experimental systems of interest, as discussed in section 1.1, is alloy nanoparticles of germanium and gold or tin. However, using the current framework, this system would be very difficult to model. Instead of the rates depending only on the size of the parti-

cle, they would depend on the composition as well; additionally, the eutectic phase diagram gives more complicated melting and freezing behavior, meaning more phases than fully-solid and fully-liquid particles must be tracked[46]. Generating and solving one rate equation per size, composition, and phase very quickly becomes infeasible, so a different framework such as kinetic Monte Carlo would be better suited to modeling this system.

2.8 Rapid Thermal Annealing Model

In the same framework as the PLM model and the ion beam synthesis model before it, it is fairly trivial to build a model of the RTA process. In the physical system, a heat lamp whose light is absorbed primarily by the silicon substrate is used to heat the sample; typical anneal times are about ten seconds with a temperature ramp-up and ramp-down of two seconds, and the temperatures used are a few hundred degrees Celsius depending on the sample. Melting, laser absorption, and so on are not relevant here, and the process is sufficiently slow (on the scale of ten seconds) that the temperature is essentially uniform within the particles and implanted layer. The RTA model thus keeps the nucleation, growth and coarsening processes (absorption and desorption of dissolved atoms) in the limit of uniform temperature and diffusion constant, where the diffusion-reaction equation is analytically solvable[6, 21]. A temperature schedule is imposed to mimic the RTA process. This subsidiary model allows generation of annealed starting distributions to begin PLM from, simulation of the effect on the particle size distribution of annealing after PLM, and simulation of cycling PLM and RTA steps to judge the feasibility of new phase-change memory devices.

2.9 Injection Model

Another model that is fairly trivial to build from the PLM and ion beam synthesis models concerns the colloidal chemistry process of "size-focusing"[8], where fast growth of nanoparticles and size-distribution narrowing is achieved by secondary injections of reactants after growth has begun. The real wet-chemistry process is complicated by the dynamics of injecting and stirring fluids, and by the effects of the surfactant on the absorption and desorption of atoms; however, a simple model may still capture the size-focusing effect. This model is built, similar to the RTA model, by keeping only the constant-temperature coarsening terms, and adding a rate of monomer injection which is externally controlled. The rate equation for dissolved atoms in this model is:

$$\frac{d\langle n_1\rangle}{dt} = F(t) - 2D\sigma_1\langle n_1\rangle^2 - D\sum_{j>1}\sigma_j\langle n_1\rangle\langle n_j\rangle + 2\frac{\langle n_2\rangle}{\tau_2} + \sum_{j>2}\frac{\langle n_j\rangle}{\tau_j} \tag{2.45}$$

and for all other particles the same rate equations as 2.20 are used. $F(t)$ is the flux of injected atoms, which is set by the user. Setting F to be a square wave on the timescale

of seconds mimics multiple secondary injections, while a constant F mimics a continuous stream of dissolved atoms or reactants being added to the system.

Chapter 3

Results of the Model

3.1 General Result

The first results of the model are a simulation of a prototypical PLM experiment: 0.3 J/cm^2 laser fluence, 30 ns pulse length, on Ge particles at 6 atomic percent concentration in the matrix. For this system, the peak temperature reached is nearly 3000K, starting from room temperature. The temperature in the implanted layer as a function of time is shown in figure 3.1.

An interesting feature of these results is the cooling rate in the implanted layer, which is 2×10^{11} K/s for the first nanosecond, and over 3×10^{10} until the particles are fully solidified and the distribution effectively stops changing at around 400°, 90 ns after the laser pulse ends. This quench rate is comparable to calculations of the quench rate for PLM of thin films[17, 19]. It is worth noting that this quench rate is fast even on the time scale of phonons, raising questions about the validity of the classical heat transport approach; however, the results are reasonable with respect to experimental observations, including amorphization and mixing of eutectic alloy nanoparticles[11], which requires a very fast quench. Such high quench rates arise from a high temperature gradient in the material, due in turn to the portions of the material that absorb the laser heating quickly while adjacent material is relatively unaffected. In the thin film geometry, the surface is heated to a depth related to the absorption length of the laser light; in the nanoparticle geometry in a transparent matrix, only the particles are heated. It may be expected therefore that the quench rate depends on a large temperature gradient from the particle to the surrounding matrix, and that this quench rate may even be faster than in the thin film geometry due to the small size of the particles. However, examination of the heat transport results shows that the temperature difference between the particles and the surrounding matrix is never greater than a few degrees; the matrix in the implanted layer reaches essentially the same high temperatures as the particles. The fast quench rate arises, similar to the thin film case, from the one-dimensional heat transport between the implanted layer and the adjacent unimplanted layers of silica.

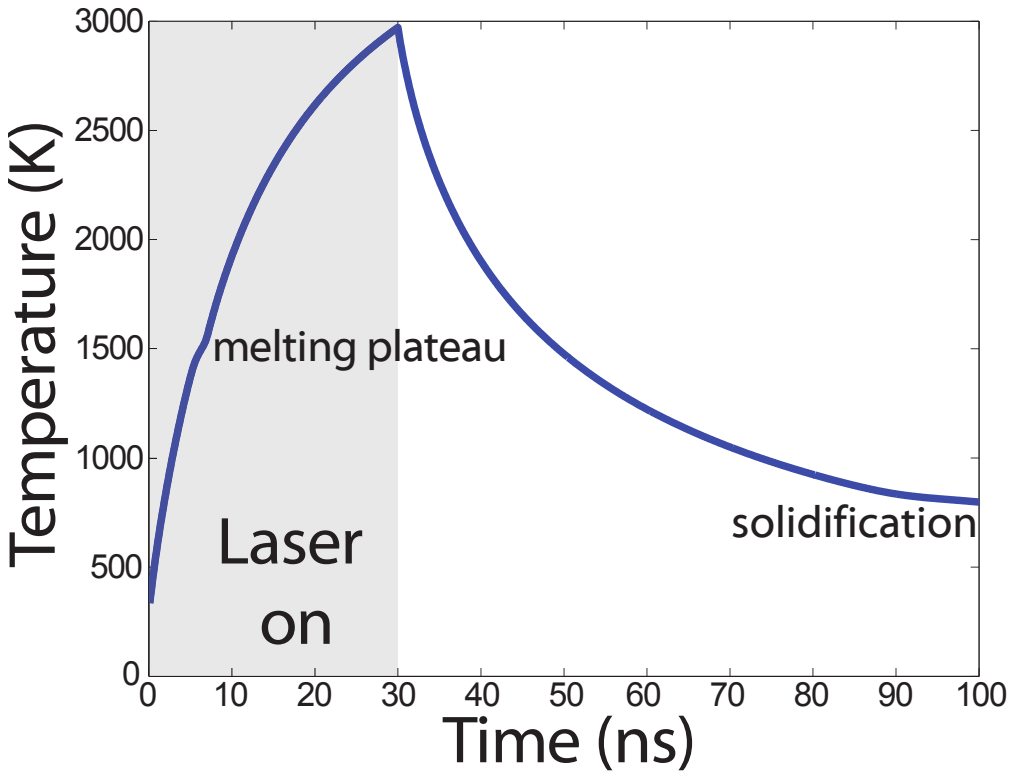

Figure 3.1: Temperature profile over time for a prototypical 0.3 J/cm^2 laser fluence PLM at 0.5 J/m^2 Ge-matrix interface energy. The melting plateau due to the latent heat can be observed, and the beginning of a solidification plateau is visible after 90 ns.

3.2 Testing Assumptions

Interface Energy

The most drastic assumption made is reducing the Ge-silica interface energy. In the model of ion-beam synthesis, this was found to set a scale for the average particle size, while the scaled shape of the distribution was unaffected[21]. The interface energy has a size-scaling effect because it controls the critical nucleus size for formation of particles out of the supersaturated matrix; a larger critical nucleus in IBS leads to a proportionally larger average cluster size. However, the effect of increasing the interface energy in PLM is more complicated, as shown in figure 3.2 for a laser fluence of 0.15 J/cm^2 and interface energy between 0.2 and 0.8 J/m^2. The different simulations behave similarly at the beginning of the simulation, with the particles absorbing light, heating up, melting, and beginning to dissolve into the matrix. In the smallest interface-energy case, the particles dissolve entirely; at the peak temperature there is a dynamic equilibrium between dissolved atoms and liquid clusters of fifty or fewer atoms. As the sample cools, these tiny clusters grow into a unimodal distribution with a small average size.

For larger interface energies, the particles melt and begin to dissolve into the matrix, but there is a substantial barrier to nucleation of small new clusters, driving dissolved atoms back into the large liquid particles. The peak concentration of dissolved atoms increases with interface energy, and the concentration of small clusters at the peak temperature drops. In the case of 0.5 J/m^2 interface energy, some dissolution occurs, but an equilibrium is reached between large liquid particles and dissolved atoms with virtually no nucleation of small clusters. As the sample cools, some of these dissolved atoms rejoin the large particles, and the large particles grow; other dissolved atoms nucleate small particles, forming a second peak in the size distribution for a final result that is strongly bimodal.

Although quite computationally expensive, a simulation with 0.8 J/m^2 interface energy, which is a realistic value[4], may be performed at this reduced laser fluence. In this case virtually no nucleation of new clusters occurs, and the final distribution is composed entirely of particles that grew by coarsening during the initial heating, melted, and mostly maintained their size through the rest of the laser pulse, growing again as the sample cooled and dissolved atoms rejoined the particles. The final distribution is thus unimodal, and has a much larger average size than the simulations with lower interface energy.

The large differences between the results at different interface energies are somewhat disheartening, in that results for the easily-calculated small interface energies cannot be straightforwardly scaled to predict results for the realistic interface energy. However, based on this comparison, insight into the behavior of the real system may still be drawn from the small interface energy simulations, especially by comparing two different energies.

Uniform Implanted Layer

In the model, the variations in concentration and heating with location in the sample are ignored; in reality, there is a non-uniform implant profile[21], and laser absorption by the top few particles decreases the light available to particles situated deeper in the sample. Testing the effect of the concentration profile is non-trivial, as this will affect the development of the particle size distribution during implant; however, it is fairly simple to test the depth-dependence of the PLM process starting from a uniform concentration profile. Instead of having one implanted layer, the implanted layer is broken into several adjacent sub-layers. Each of these sub-layers is treated according to the model above, except that the incident laser power is modified by the other implanted sub-layers, and the 1D interlayer heat transfer problem is modified accordingly. Each sub-layer has an average matrix temperature that is independent of the other layers, and each has its own particle population being tracked separately. Layers are allowed to transfer dissolved atoms by a finite-difference version of the diffusion equation.

The results, shown in figure 3.3 for five sub-layers, with an interface energy of 0.2 J/m^2 and a laser fluence of 0.15 J/cm^2, are encouraging; there is little difference in the temperatures experienced or the final particle size distributions amongst the different sub-layers, and the results are also very similar to the uniform-layer simulation results (black lines). The dominant effect on the temperature appears to be heat transport out into the unimplanted

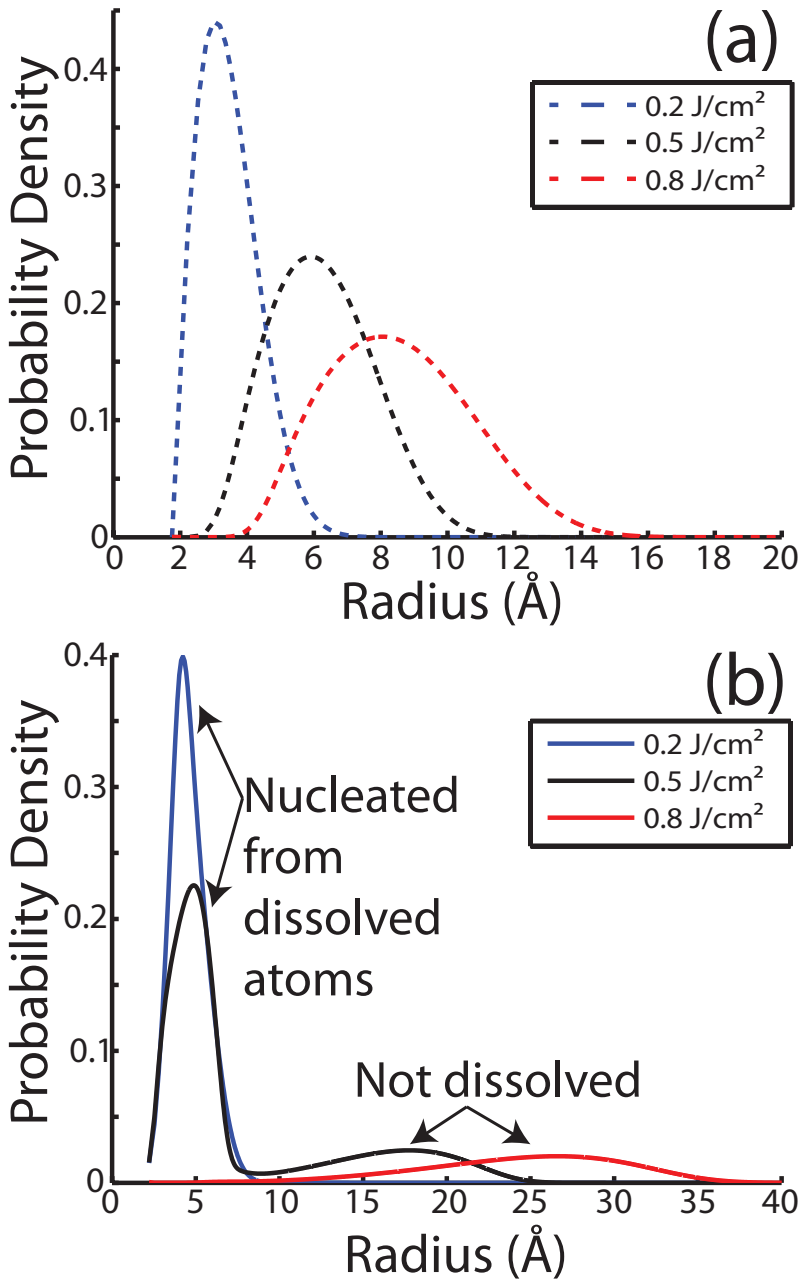

Figure 3.2: Comparison of the size distribution results at different interface energies, after ion beam synthesis (a) and after PLM with a laser fluence of 0.15 J/cm^2 (b). The results of ion beam synthesis show a straightforward scaling of the particle size (as discussed in ref. [21]), but the results of PLM are slightly more complicated, running from unimodal to bimodal and back to a unimodal distribution with increasing interface energy. The blue curves have an interface energy of 0.2 J/m^2, the black curves 0.5 J/m^2, and the red curves 0.8 J/m^2, the value estimated in ref. [4]. Dissolved atoms are omitted from the distributions. Note that the two plots are on different scales.

silica, as the top and bottom layers are cooler than the middle layers; no effect of the upper layers screening the laser from the lower layers is seen. The maximum difference in temperature between the layers is 170K just at the end of the laser pulse; while this may seem like a significant difference, the similarity of the final particle size distributions indicates that it is not. The final distributions show an increase in width from 40% in the top layer to 46% wide in the deepest layer, compared to 47% in the single-layer simulation; the final average size also increases slightly with depth from 4.4 to 4.6 angstrom. This is likely attributable to the slightly slower cooling rate observed in the deeper layers, as slower cooling gives more time for coarsening to widen the distribution. These differences amongst the sub-layers, however, are quite small, justifying the approximation of a uniform layer, at least while the larger errors due to the interface energy and other approximations exist in the model.

3.3 PLM - RTA Cycle

One of the major motivations of this project was to judge the long-term stability of a phase-change memory system based on cycling PLM and RTA in embedded nanoparticles. Although the real phase-change system envisioned would be constructed of binary alloy nanostructures[11], some insight into the stability may be found by analysis of the single-species model. The first results used an interface energy of 0.2 J/m^2 and were very encouraging; see figure 3.4(a). In this case, the PLM step acts to erase all previous effects on the size distribution; the final distribution is the same whether the starting distribution was as-implanted, annealed for various times, or annealed from a prior PLM step. This implies perfect stability in the particle size distribution, although concerns about diffusion of the implanted species to the device surfaces, mechanical stability, and other issues are not addressed.

The results of cycling at a higher interface energy of 0.5 J/m^2 are less encouraging; the average particle size grows with every cycle, as shown in figure 3.4(b). This indicates that the particle size distribution is not stable to repeated PLM/RTA cycles and thus not suitable for phase change memory applications. However, the change in average size is decreasing with each cycle, suggesting that the particles may stabilize at a larger size; exploring this possibility is infeasible with the current model due to the high computational costs for particles larger than a few tens of thousands of atoms. Using a higher energy laser pulse may also help, as in the limit of high fluence, the particles must fully dissolve into the matrix; however, whether this is achievable without entirely destroying the sample is not clear. Overall, the results for possible phase-change memory devices are inconclusive.

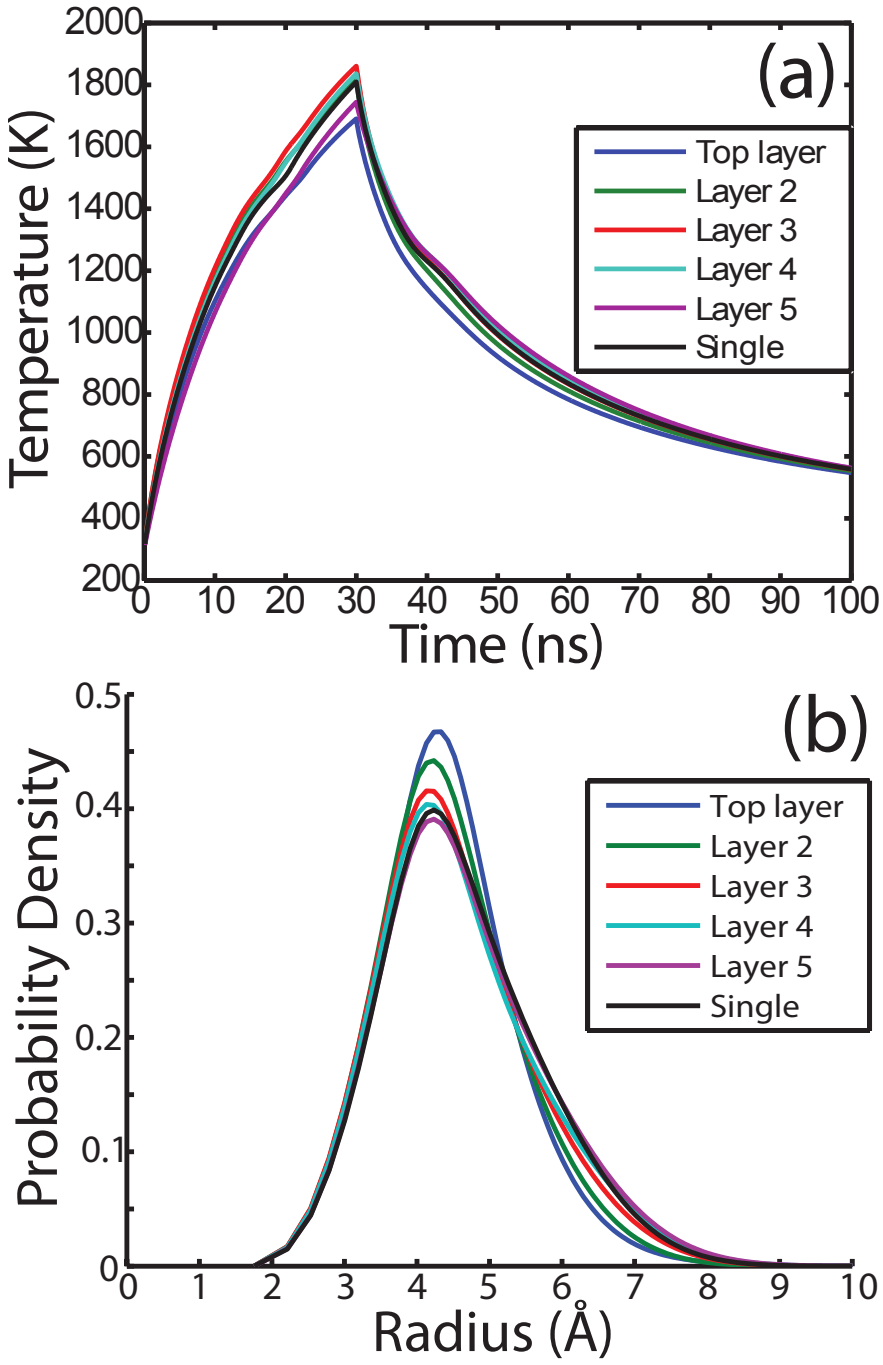

Figure 3.3: Temperature profiles (a) and final particle size distributions (b) for the simulation in which the implanted layer is broken into five sub-layers (colors), compared to the results of a single-layer simulation (black). Layers are numbered from the top down; layer 1 in dark blue is closest to the air and layer 5 in purple is closest to the silicon substrate.

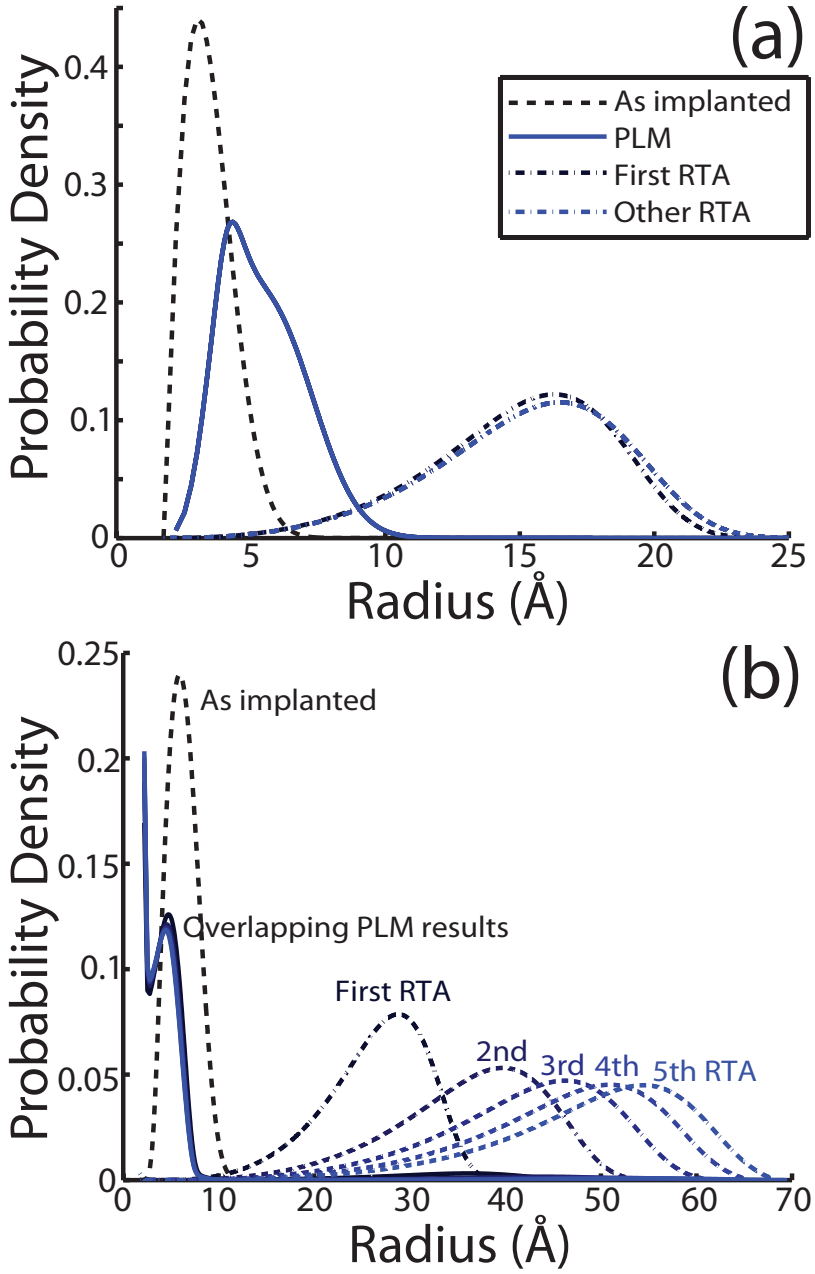

Figure 3.4: Final size distributions, as-implanted and at the end of each PLM and RTA step in 5 cycles, for interface energy 0.2 J/m^2 (a) and 0.5 J/m^2 (b). The RTA step is 4 seconds at 300°C, and the PLM uses a fluence of 0.3 J/cm^2. For the lower interface energy, the size distributions at the end of each PLM step and every RTA step after the first exactly overlay each other, indicating good stability of the particle size distribution under repeated PLM/RTA cycling. The results for the larger interface energy are not as encouraging.

3.4 Variation of Parameters

Laser Fluence

Experimentally, the laser fluence in the PLM system is fairly easy to modify by placing attenuators or filters in the path of the beam. Lower fluences are therefore of some interest. By systematically lowering the fluence in simulation, three distinct regimes can be identified based on the characteristics of the final size distribution and phase information. In the high fluence regime, which includes the 0.3 J/cm^2 standard PLM through roughly 0.15 J/cm^2, virtually all of the particles melt. The final distributions, depending on the interface energy, are those discussed in section 3.2: broad size distributions, including one or both of 1) a peak due to re-nucleation of dissolved atoms, and 2) a peak due to clusters that grew during heating, melted and maintained their size. In the low-fluence regime, below about 0.1 J/cm^2, no melting occurs and the final distribution resembles that after a short anneal: the average size has increased slightly and the distribution shape is between the starting shape and the standard coarsening distribution shape.

In the intermediate fluence regime, the behavior is more interesting. Both the melted-particle peak(s) from the high-fluence regime and the annealed-solid peak from the low-fluence regime appear, leading to a bimodal distribution for 0.2 or 0.8 J/m^2 interface energy and a trimodal distribution for 0.5 J/m^2 (see green curves in figure 3.5(b,d)). The peaks of particles that melted during the PLM process are fairly broad, just as in the high-fluence regime; however, the peak of particles that never melted, taken by itself, is much narrower than in the low-fluence simulations, at roughly 10% width. This narrowing of the solid peak occurs for two reasons: the melting rate is slightly size-selective (see section 2.5), with small particles melting sooner, and the particles have a ready supply of atoms which have been dissolved from the liquid particles, so they may grow without coarsening. While the overall width of these multimodal distributions is quite broad, an annealing scheme to take advantage of the narrowing effect is discussed in section 4.1.

It should be noted that the simulation results are quite sensitive to the laser fluence. The window in which the 'intermediate fluence' regime is seen is small, between 0.112 and 0.125 J/cm^2 inclusive (although there is a much wider range of acceptable fluences at 0.2 J/m^2 interface energy). Within this regime, the higher the fluence, the greater the narrowing of the solid-particle peak. This presents some challenge for experimental validation, as the power delivered by the laser may fluctuate and be difficult to control to this precision.

Pulse Width and Repetitions

Besides the fluence, several other characteristics of the laser can be varied, if only by changing laser systems. The laser wavelength, pulse width, and number of pulses may be varied in addition to the total fluence. Changing the laser wavelength is not terribly interesting; as long as the particles absorb the light while the matrix is transparent, the fluence can be adjusted to give the same heating. The absorption cross section according

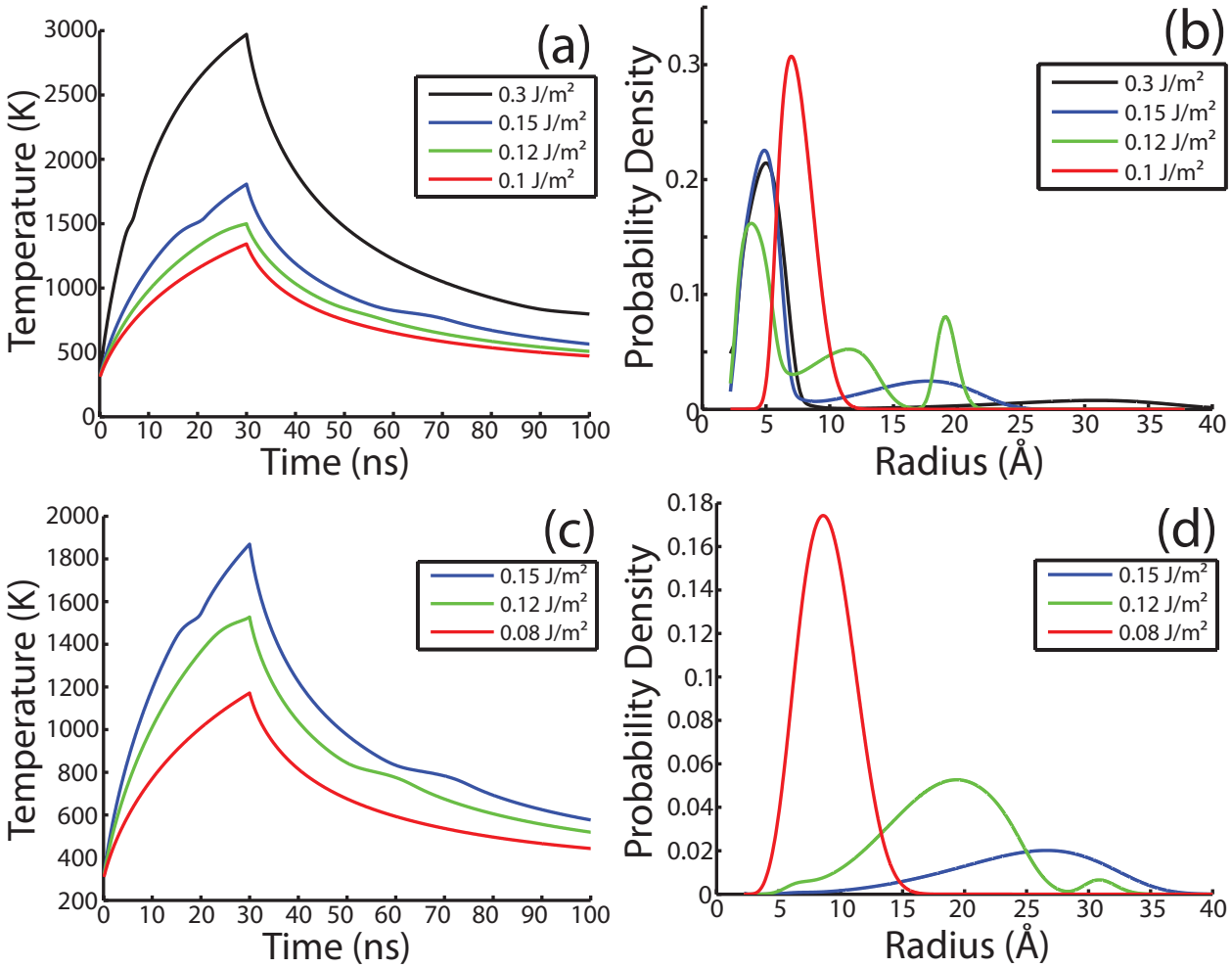

Figure 3.5: Temperature profiles (a,c) and final particle size distributions (b,d) for various laser fluences at an interface energy of 0.5 J/m^2 (a,b) and 0.8 J/m^2 (c,d). Three distinct regimes emerge: the high fluence regime, in which all particles melt, the low fluence regime, in which nothing melts, and the intermediate fluence regime in which some particles melt while others remain solid. Latent heat plateaus in the temperature plots indicate whether melting has occurred. Dissolved atoms at the end of the simulation are omitted.

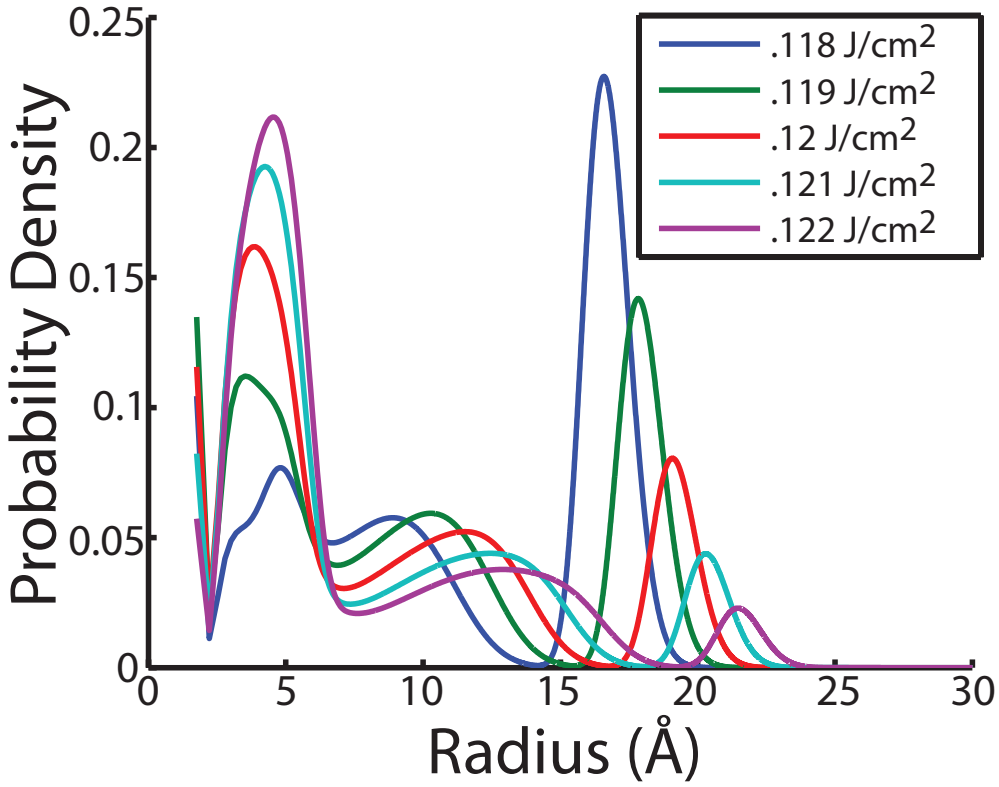

Figure 3.6: Particle size distributions at various laser fluences close to 0.12 J/cm^2, at an interface energy of 0.5 J/m^2. The final distribution is extremely sensitive to the laser fluence.

to the Mie theory is proportional to the volume regardless of the wavelength, so the size-selectivity of the heating will not change.

Changing the pulse width while keeping the total fluence constant shows that the fluence is not the only thing controlling the final distribution. For a short pulse, there is less time to dissipate the heat of the laser, so the peak temperature is higher than for a longer pulse at the same total fluence. The final distribution resembles the result of raising the fluence at a constant pulse width. Similarly, a longer pulse gives a similar result to lowering the fluence. This can be seen in figure 3.7(b), where distributions at varied fluences are overlaid with distributions at varied pulse widths.

Adjusting the fluence along with the pulse width allows a more direct comparison of the results, although it is somewhat difficult to match the fluences. At a given pulse width, increasing the fluence increases the number of particles that melt and the size of the particles that stay solid simultaneously; the resulting size distributions' large-particle peak moves to larger R and gets shorter (see figure 3.6). Changing the pulse width and fluence together, the particle size of the large-particle peak can be matched up (see figure 3.8); in this case the height of the large-particle peak increases with increasing pulse width. Similarly, matching

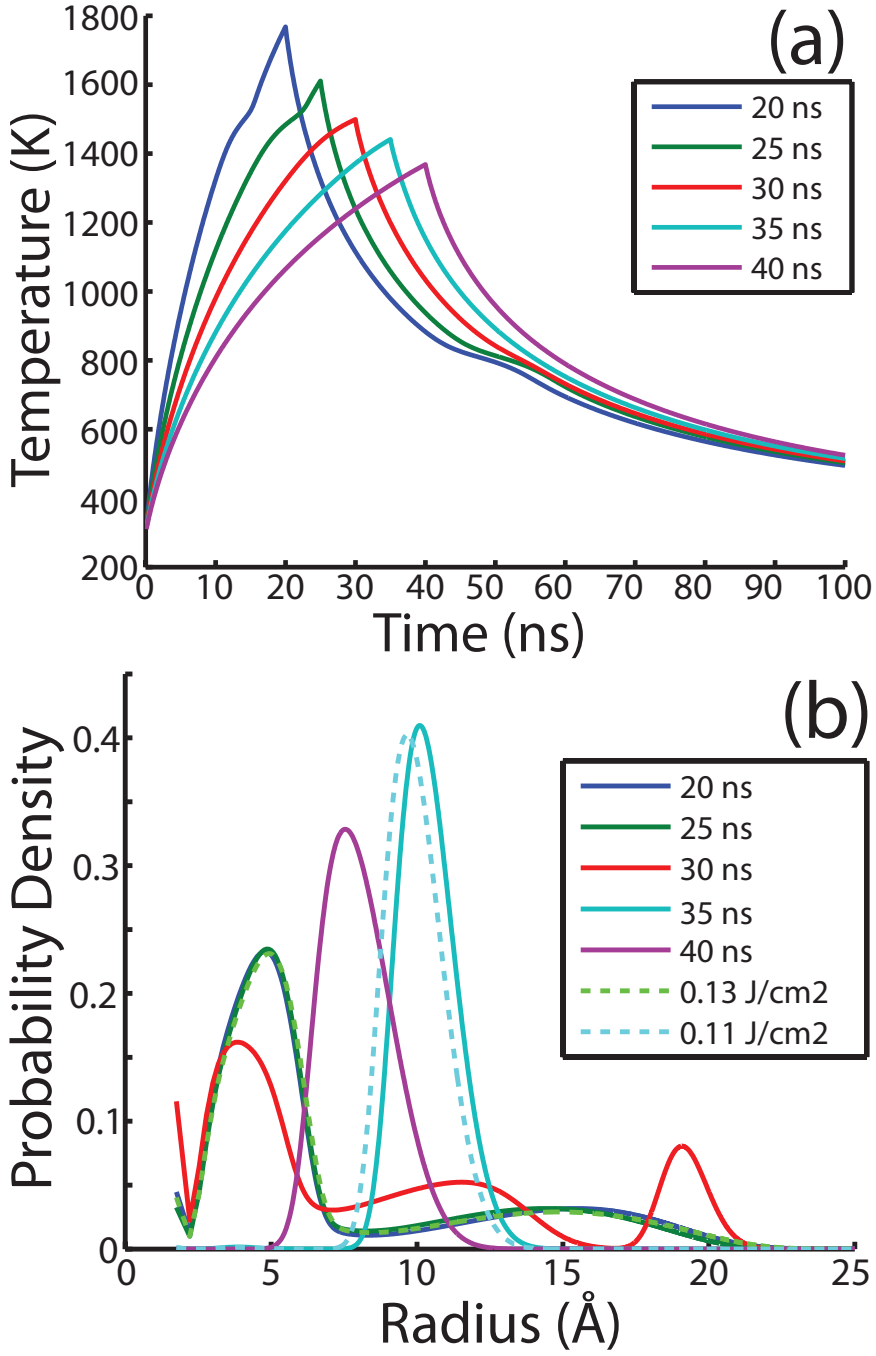

Figure 3.7: Temperature profiles (a) and final particle size distributions (b) for various laser pulse durations at constant total fluence. The laser fluence is 0.12 J/cm^2 and the interface energy is 0.5 J/m^2. Shortening the pulse pushes the final distribution into the high-fluence shape, and lengthening the pulse gives the low-fluence shape, as illustrated by the dotted lines from simulations at the same pulse width (30 ns) but different fluences.

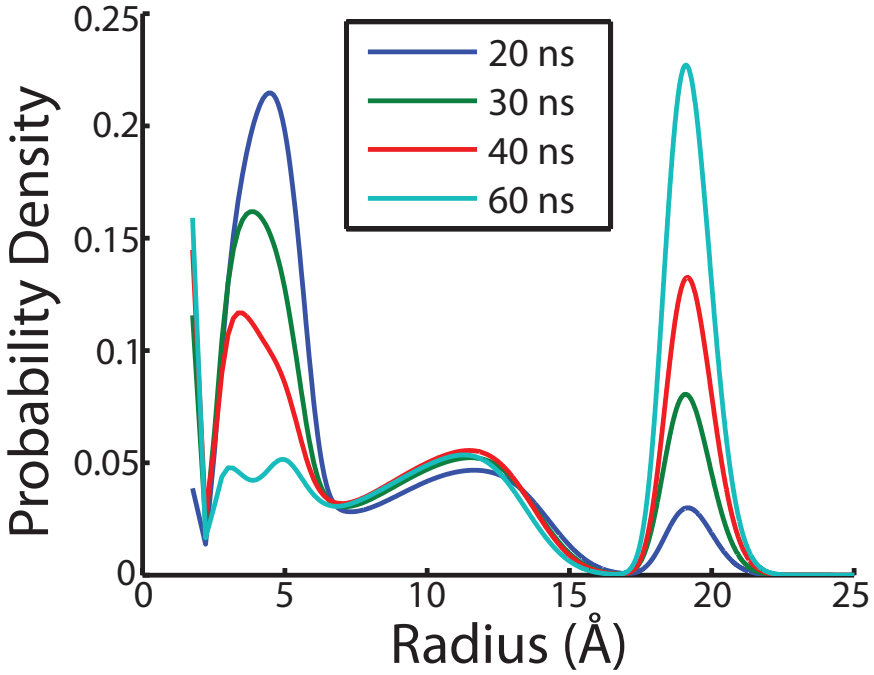

Figure 3.8: Particle size distributions for various laser pulse durations, changing the fluence to line up the size of the large particles. The laser fluences are 0.1, 0.12, 0.139, and 0.175 J/cm^2 for the 20 ns, 30 ns, 40 ns, and 60 ns pulses respectively.

up the heights of the large-particle peak moves this peak to larger particle sizes with increased pulse width. In other words, the size of the large particles and their relative number can be controlled independently using the fluence and pulse width together.

Many experimental PLM systems are set up to deliver repeated pulses at a pulse rate of roughly 1-10 Hz[14, 15]. At these pulse rates, the simulation results show that the pulses are independent in terms of buildup of heat; 200 ns after a 0.3 J/cm^2 laser pulse begins, the temperature has dropped back to 230°C from a peak temperature of 2700°C, so 10^8 nanoseconds later when the next pulse begins, the heat remaining from the first pulse will be negligible. However, multiple pulses will have cumulative effects; for low-fluence or high-fluence pulses at high interface energy, each pulse will anneal the sample distribution a little more. High-fluence pulses at low interface energy will re-set the size distribution after every pulse, leading to no cumulative effect. For repeated pulses in the intermediate fluence regime, each pulse melts a fraction of the particles which then maintain their size or shrink slightly, while some particles remain solid and grow. The kinetics of melting make it somewhat size-selective, where small particles tend to transform more readily than large particles, so it may be expected that the previous pulse's solid particles will remain solid and continue to grow through the next pulse. However, the size-selectivity is in reality very weak; a portion of each of the peaks in the starting distribution remains solid. This leads to a corrugated-looking

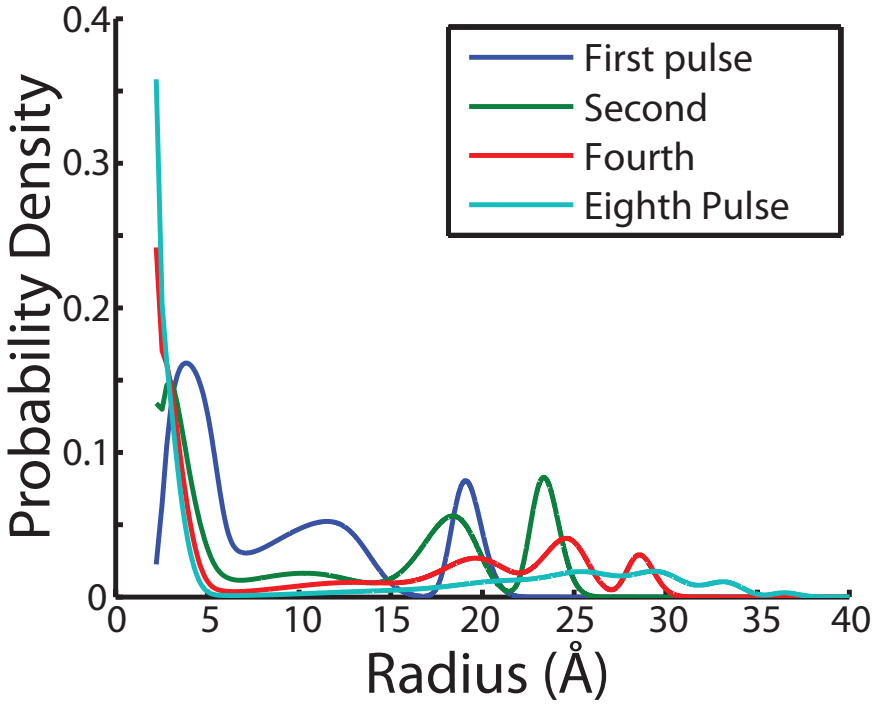

Figure 3.9: Size distributions after repeated laser pulses in the intermediate-fluence regime (0.12 J/cm^2). Dissolved atoms are omitted.

final distribution after several pulses, in which several relatively sharp and well-separated peaks sit atop a broad background (see figure 3.9); the sharp peaks comprise the particles that were solid throughout the most recent pulse, while the background is particles that melted. Eventually, the corrugations are washed out into a single, extremely broad peak.

Particle Concentration

All of the results thus far use the same concentration of germanium in the matrix, 0.004 atoms per Å^3 or roughly 6 at%. This is a typical concentration for ion implantation[24], but higher and lower concentrations are accessible by changing the implant dose or using another technique such as cosputtering of Ge and silica to form the embedded particles. Changing the concentration has two effects: more germanium in the matrix gives more laser absorption, and increasing the concentration of particles shortens the length scale of the coarsening problem.

The fluence can be changed to partially compensate for the difference in absorption. The absorption cross-sections of the particles are proportional to their volume, so to first order, the fluence should be varied as the inverse of the total volume to compensate; however, the attenuation over the film thickness and the reflection and absorption at the silicon substrate makes this less straightforward. In particular, when the implanted layer is sparse enough that

a significant amount of heating occurs at the silicon substrate surface, heat is transported from the silicon layer into the implanted layer, changing the shape of the temperature profile (see figure 3.10(a)). Additionally, changing the concentration of particles makes the melt plateau in the temperature curve more or less pronounced.

A set of simulations were run with concentrations ranging from one-quarter to four times the standard dose, with fluence adjusted by hand to make the temperature profile over the first 10 ns of the simulation as similar as possible. The results of these simulations are presented in figure 3.10. Despite the fluence adjustment, the peak temperature of the simulation decreases with increasing concentration; the curvature of the temperature profile while the laser is on increases with increasing concentration. The fraction of the particles that are liquid at the peak temperature drops with concentration; the simulation at one-quarter the standard concentration shows complete melting (>99% by mass, excluding the nominally-solid dissolved atoms), while all higher concentrations have a distinct peak in the final distribution from solid particles (for the half-dose case, this is barely visible, centered at 23 Å). As the concentration increases, this solid peak becomes larger as a fraction of the total number of particles, and its average radius decreases. At the highest concentration, four times the standard dose, the final size distribution is very similar to the low-fluence regime, but in this case a significant fraction of the particles (20%) melt; because of the shorter length scale for coarsening, the smaller particles that melted are consumed entirely while the sample is cooling down. The final particle size distribution is significantly narrower, at 17% wide, than the starting distribution (64% wide). The reason for this narrowing will be discussed in the next chapter.

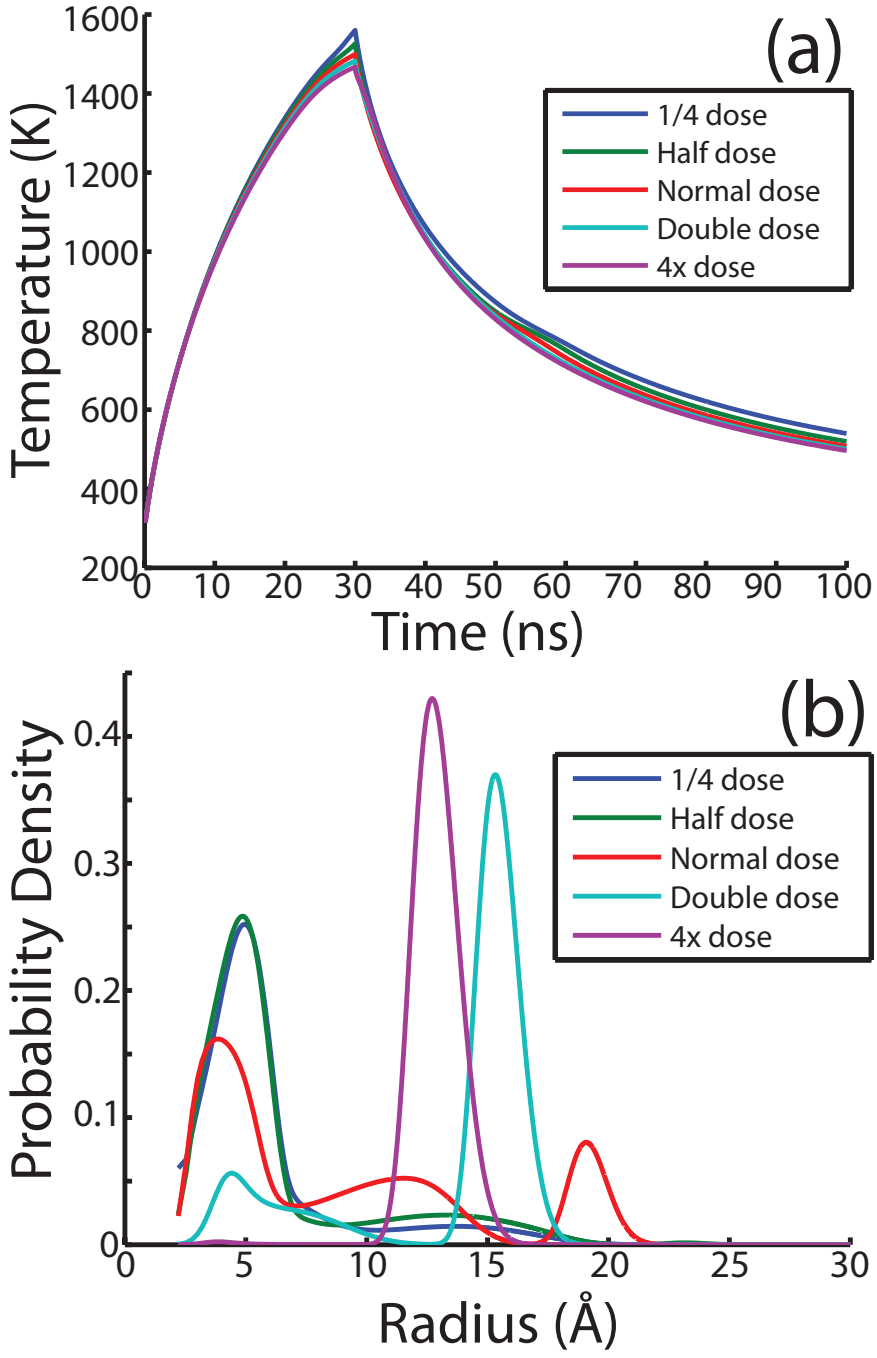

Figure 3.10: Temperature profiles (a) and final particle size distributions (b) for various germanium concentrations ranging from 0.001 to 0.016 atoms/Å^3, with fluence tuned to give a temperature profile as close to the 0.12 J/cm^2, 0.004 atoms/Å^3 case as possible.

Chapter 4

Theory of Size Distribution Narrowing

4.1 Recipe for Narrowing by PLM and RTA

In section 3.4 it was shown that a pulsed laser melting experiment at reduced laser fluence leads to a distribution that is split into several well-separated peaks. Further, it was shown that the peak of the large-radius particles was quite narrow taken on its own. While this multimodal distribution is itself quite broad, this peak's narrowness suggests a method for achieving an overall narrow distribution.

For long anneal times, second-phase particles are known to asymptotically approach a steady-state distribution whose shape is independent of the starting distribution[47] and quite broad. However, the transient states that the distribution passes through between initial and steady-state shapes do depend on the starting distribution, and the size distribution may be arrested in any of its transient states by controlling the annealing time and temperature. For unimodal distributions, the distribution width will usually progress monotonically from the original to the final width[48], but multimodal distributions can exchange mass between distribution peaks and thus have more interesting behavior.

Simulating a short anneal starting with the results of the intermediate-fluence PLM simulation gives very promising results (see figure 4.1): the final width of the distribution is just 12%. The optimal anneal for the 0.5 J/m^2 interface energy simulation was found to be about "0.2 seconds" at 300°C; the anneal was assumed to have a 2-second linear temperature ramp to heat up and cool back down, and significant annealing takes place during the ramp up to temperature. During the anneal, mass is transferred from the broad small-particle peaks to the narrow large-particle peak, which grows without significant broadening as long as smaller-particle peaks exist. In fact, this peak narrows somewhat during the early part of the anneal, from 9.8% to 9.6% wide, before broadening to 12% in the final stages of consumption of the small-particle peaks. After the small-particle peaks are consumed, the single remaining peak begins to broaden towards the standard coarsening distribution, but

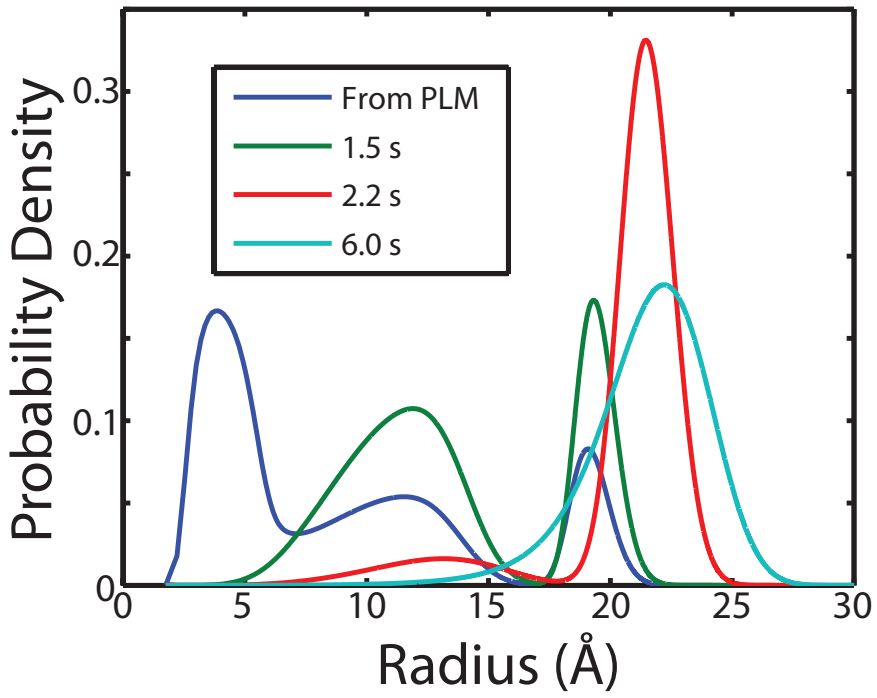

Figure 4.1: Particle size distributions during a simulated short anneal. The starting distribution from the PLM simulation, a representative distribution from the middle of the anneal, the sharpest distribution, and an over-annealed coarsening-like distribution are shown. The interface energy for this simulation was 0.5 J/m^2, the PLM laser fluence 0.12 J/cm^2, and the anneal temperature 300°C. The legend gives the time from the start of the temperature ramp-up.

if the anneal is cut off before broadening occurs, the sharp distribution is stable at room temperature.

Increasing the interface energy to the more realistic 0.8 J/m^2 gives the same qualitative behavior and a best distribution width of 15% (see figure 4.2) at an anneal time of 16.5 seconds at 300°C. Thus, the narrowing effect is expected regardless of interface energy. It is worth noting that the distribution with the narrowest nominal width may not be the most suitable for narrowing applications, as it is still bimodal; using the full width at half maximum of the distribution misses any secondary peaks whose height is lower than the half-maximum. Some judgment is thus required to find the optimal distribution; the criterion used here is that the primary peak is at its maximum height with respect to time, which is close to both the minimum of the width and to the complete disappearance of the secondary peak.

The general recipe for obtaining narrow size distributions by PLM and RTA is as follows: first, find a PLM fluence that will melt some but not all of the particles, creating a multimodal distribution with a sharp large-particle peak. Second, anneal the post-PLM samples for a

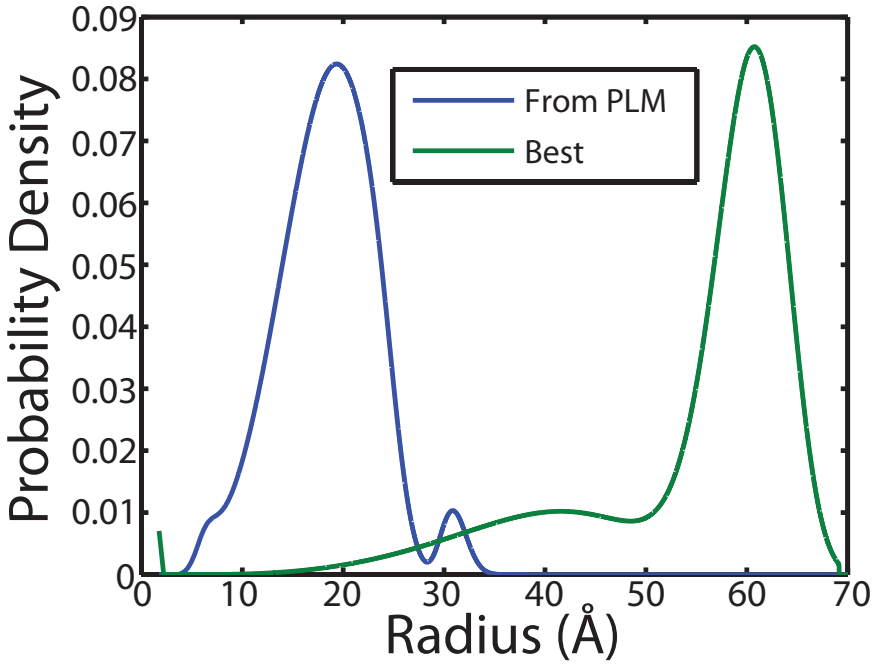

Figure 4.2: Particle size distributions during a simulated short anneal at a realistic interface energy. The starting distribution from the PLM simulation and the sharpest distribution are shown. The interface energy for this simulation was 0.8 J/m^2, the PLM laser fluence 0.12 J/cm^2, and the anneal temperature 300°C. The "best" distribution is after 16.5 seconds at temperature (18.5 from start of ramp-up).

short time, optimizing the time and temperature to just barely consume the small-particle peaks. As discovered in section 3.4, the annealing step may be skipped if the particle concentration is high enough that significant coarsening occurs in the few nanoseconds that the sample is cooling down from the laser pulse; a material system with a higher diffusion constant will also have this effect at lower particle concentrations.

4.2 Artificial Bimodal Distributions

The narrowing effect may be partially reproduced by annealing an artificially-created bimodal distribution, such as may be created physically by mixing two pre-made samples of nanoparticles with different average sizes and individually unimodal distributions. In simulation, starting distributions were created by adding two coarsening-like distributions at mean radii 8 and 20 Å and 28% individual width. The relative concentrations of the two distributions were varied, keeping the total germanium concentration constant.

With a 1:1 mass ratio of the two populations, annealing at 300°C, the best final distribution is achieved after 3 seconds' anneal, and is narrowed from 28% to 25% wide. The particles

grow to an average radius of 24 Å. With a 4:1 ratio of small particles to large particles, the narrowing and growth are more substantial; after 16 seconds' anneal the distribution is just 21% wide and the particles have grown to 33 Å average radius. In general, the more small particles there are, the more narrowing occurs and the more the large particles grow; with a 16:1 ratio the best distribution is 17% wide, its average radius is 50 Å, and it is reached after 83 seconds at temperature. Considering that the starting distributions were 28% wide, this is a quite significant amount of narrowing.

Changing the average sizes of the two starting distributions will also affect the narrowing achieved. Specifically, reducing the average size of the small particles improves the narrowing; with a 1:1 mass ratio and the large particles fixed at a starting average radius of 20 Å, a small-particle size of 3 Å leads to a best width of 22%. A small-particle size of 4 Å gives a best width of 23%, 6 Å gives 25%, and 10 Å gives no narrowing at all. The final average radius in all cases is just under 25 Å. In the limit of small particles, co-sputtering germanium and silica on top of pre-made nanoparticles would give a small-particle peak in the size range of single- or few-atom clusters, and this effect can be combined with the effect of changing the mass ratio.

4.3 Injection Model

Moving away from heat treatments, narrowing may also be achieved during growth of nanoparticles. In an effort to understand the size-focusing effect reported in colloidal chemistry[8, 9, 10], a model was built that may not be quantitatively accurate but does lend some insight into narrowing. In the model, nanoparticles nucleate and grow under the influence of repeated addition of dissolved atoms to the system. The material parameters used are those of germanium in silica, and thus not accurate to colloidal chemistry, but varying the parameters provides useful information. Unless otherwise noted, the reactant was added continuously rather than in discrete injections. All simulations were given the same total dose of material (0.004 atoms/Å^3), and all simulations were at room temperature.

For all of the test parameters, the size distribution takes on a characteristic swept shape, with a long tail to smaller particles and a sharp cutoff on the large-particle side. The average size and the width of this distribution varies, however. The final size distributions are shown in figure 4.3(a). Varying the rate at which the reactant is added (and thus the total time of the simulation to achieve the same dose) shows that the more slowly the reactant is added, the larger the particles and the narrower their distribution; the rate was varied between 10^{-6} atoms/Å^{3}s (slow) to 10^{-4} atoms/Å^{3}s (fast), compared to 10^{-5} (basic). Increasing the interface energy from 0.2 to 0.5 J/m^2 (high gamma) dramatically narrows the distribution width and gives larger particles; increasing the diffusion constant instead by a factor of 100 (high D) also leads to larger particles and a narrow distribution, but not as narrow as the interface energy case.

Finally, changing from continuous addition of reactants to a pulsed addition, with 100 times the basic dose rate for 0.2 seconds, repeated every 20 seconds, leads to much smaller

particles with a broader size distribution than the continuous case. Examining the distribution as a function of time during the simulation shows that at this temperature, particles only grow while an appreciable concentration of dissolved atoms are present, and that dissolved atoms are absorbed out of the system nearly as fast as they can be introduced; in essence this simulation is the same as a continuous addition at 100 times the basic rate. In the real system, the reactants may not be absorbed so quickly, but they may still benefit from a lower-rate, continuous addition of reactants rather than discrete injections.

Figure 4.3(b) is a parametric plot of the width vs. the average radius during the simulation. All of the simulations come close to following a common curve, and as illustrated by the dashed lines, the decline in width as the average radius increases is slightly faster than proportional to $1/\langle R\rangle$. Notably, there is no fundamental limit on the narrowness of the size distribution that can be obtained this way, until the particles become a large enough fraction of the total sample volume that they begin to encroach on each other; a minimum width of just under 2% was obtained in these simulations at 6 at% (9 vol%) total dose.

4.4 Theory of Narrowing by Split Distributions

The main obstacle to obtaining narrow size distributions comes from Ostwald ripening: as previously mentioned, coarsening asymptotes to a universal distribution shape which is quite broad. Coarsening in turn comes from the Gibbs-Thomson effect, where due to interface or surface energy, the solubility of atoms near a small particle is larger than it is near a large particle;

$$n_R = n_\infty \exp\left(\frac{\gamma\Omega}{kTR}\right). \tag{4.1}$$

where n_R is the solubility outside a particle of radius R. This sets up a concentration gradient between small and large particles that favors growth of large particles and dissolution of small particles, which in turn broadens the size distribution. For true narrowing, small particles would need to grow while large particles shrink; this may be obtainable with growth that is not diffusion limited, or under some peculiar circumstances, but would be difficult and is not what is giving the narrowing reported thus far.

What can be done is to create a "feedstock" of small particles which are well separated in size from the large particles. The effect of this feedstock is to decrease the critical size for particles to grow instead of dissolving, such that all of the particles in the large-particle group will grow, and only the feedstock will dissolve. The dissolving feedstock creates a steady supply of dissolved atoms which leads to the large particles all growing, and at close to the same growth rate in terms of the number of atoms absorbed per unit time.

Scaling by the Average Radius

What gives the narrowing, if all the large particles are growing at the same rate, is principally that the width is reported in terms of the fraction of the average size. Defining

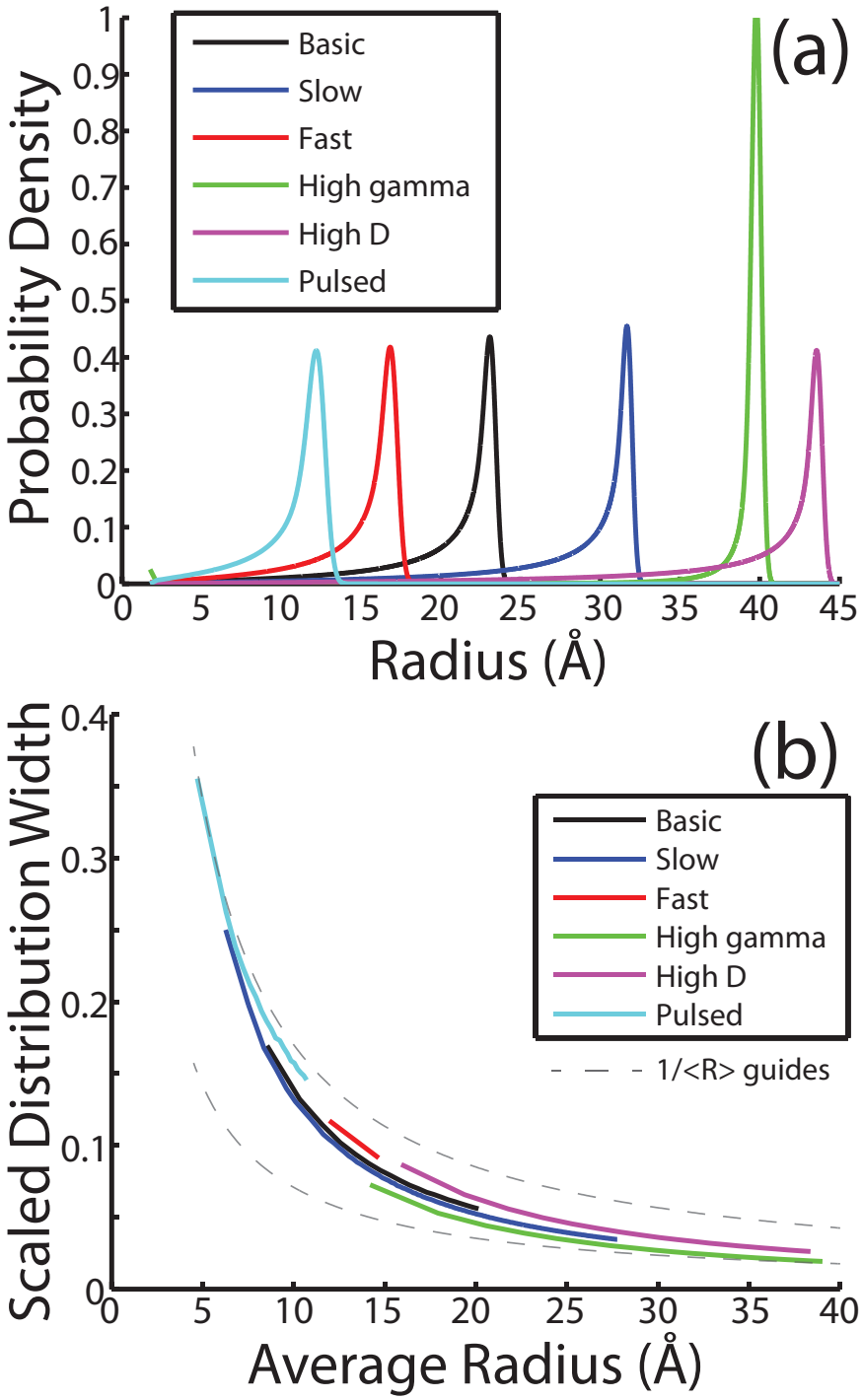

Figure 4.3: Particle size distributions (a) and a parametric plot of the distribution width vs. the average radius over the course of the simulation (b); over time the distributions proceed from left to right (increasing $\langle R \rangle$). See text for an explanation of the different simulation parameters.

the width by $W = \frac{\Delta R}{\langle R \rangle}$, where ΔR is the absolute width and $\langle R \rangle$ is the particle average radius, if ΔR were to remain constant, then W is simply proportional to $1/\langle R \rangle$. This is the cause of the parametric plot, figure 4.3(b), showing close to a $W \propto 1/\langle R \rangle$ dependence. If it is not constant, then the change in scaled width with time is

$$\frac{dW}{dt} = \frac{1}{\langle R \rangle}\frac{d\Delta R}{dt} - \frac{\Delta R}{\langle R \rangle^2}\frac{d\langle R \rangle}{dt}. \tag{4.2}$$

If $\frac{dW}{dt} > 0$, the size distribution is broadening; if $\frac{dW}{dt} < 0$, the distribution is narrowing. The faster the average radius is growing, all else being equal, the more narrowing occurs. This is in some sense not "real" narrowing, as the absolute distribution width does not necessarily decrease, but it is an important effect to bear in mind when reviewing widths reported in the literature which are given in terms of percent of the average size.

Volume vs. Radius Growth

While the scaling by the average radius explains a large chunk of the narrowing, it is not the only effect. The unscaled width ΔR is not generally constant, and may decrease over time. Some second effect is necessary to explain the plots in figure 4.3(b) narrowing faster than the $1/\langle R \rangle$ guide lines. This effect is a simple geometric factor: a single atom (a unit of volume) added to a large particle increases its radius by less than the same atom added to a small particle. Thus if all particles are absorbing atoms at close to the same rate, large particles grow more slowly in radius than small particles, and narrowing occurs. If s is the number of atoms and Ω the atomic volume, the radius is

$$R = \sqrt[3]{\frac{3\Omega}{4\pi}}s. \tag{4.3}$$

If ds/dt is the rate at which clusters are absorbing atoms, independent of s, the rate of change of the absolute width is

$$\frac{d\Delta R}{dt} = \frac{d(R_2 - R_1)}{ds}\frac{ds}{dt} = \frac{1}{3}\sqrt[3]{\frac{3\Omega}{4\pi}}(s_2^{-2/3} - s_1^{-2/3})\frac{ds}{dt} = \frac{\Omega}{4\pi}(R_2^{-2} - R_1^{-2})\frac{ds}{dt} \tag{4.4}$$

where R_2 and R_1 are the radii at which the distribution value is half its maximum, $R_2 > R_1$, and s_2 and s_1 are the numbers of atoms that correspond to the radii R_2 and R_1. This change in the absolute width over time is negative if ds/dt is constant, giving narrowing. This effect is discussed as the main reason for narrowing in the size-focusing method[8]; although ds/dt is not constant in this situation, it is sufficiently close to a constant that significant narrowing in the absolute width occurs.

A small simulation in which an initial particle size distribution grows at constant ds/dt gives an absolute width proportional to $1/\langle R \rangle^2$, and this effect combines with the effect of scaling by the average radius to give a scaled width proportional to $1/\langle R \rangle^3$ in the best case. Due to the Gibbs-Thomson effect, however, this ideal narrowing is not achieved by any of the simulations given above or by experimental results[8].

Distribution Splitting

The effects of scaling by the average size and of s-vs.-R growth are in principle quite strong, but the Gibbs-Thomson effect reduces the narrowing achievable. For this reason, it is desirable to tailor the starting distribution to get the best possible narrowing. The simulations in section 4.2 indicate that good starting distributions have two widely-separated peaks, with the small particles far outnumbering the large particles, and with the large-particle peak being as narrow as possible. This kind of starting distribution can be created by manually mixing particles with known size distributions, or by adding reactants (in effect, small particles) to already-nucleated particles in solution. It can also, as shown in section 4.1, be created using pulsed laser melting of already-synthesized nanoparticles embedded in a matrix.

Using PLM, the bimodal (or multimodal) distribution is given by a fluence for which some but not all of the particles melt. The ratio of small to large particles can be increased by increasing the fluence within this fluence range, making more particles melt and shrink. The separation of the peaks, and the size of the small particles, is largely controlled by the interface energy, as shown in section 3.2; however, it can be modified by changing the duration of the laser pulse as well (see section 3.4). The narrowness of the large-particle peak is partly due to the size-selectivity of the melting transition, where small particles melt sooner on average than large particles. The distribution splitting could be strengthened, according to section 2.5, by choosing a nanoparticle material with a larger heat of fusion relative to the heat of vaporization. Additionally, the large-particle peak is narrowed because it grows significantly, with a feedstock of dissolved atoms, during the laser pulse and immediate cooling; it exhibits narrowing from the scaling and s-vs.-R growth effects. The higher the fluence within the partial-melting regime, the more the solid particles grow, and the narrower the large-particle peak becomes.

This effect is similar to an observation made in heteroepitaxial island growth[49], where strain-induced morphology changes cause narrowing. In this case, the particle shape change is strongly size-selective, and it creates a discontinuity in the chemical potential of the particles as a function of size, similar to the difference in heat of formation between solid and liquid particles discussed in section 2.5. The size-selective transition splits the particle size distribution, and transformed large particles quickly consume untransformed small particles. The small particles provide a feed-stock for growth of the large particles, giving a narrow final distribution.

Chapter 5

Conclusions

A model of pulsed laser melting of embedded nanoparticles has been developed and used to study the evolution of particle size distributions under pulsed-laser processing. The Mie theory of light absorption, a multiscale model of heat transport, and rate equations for particle nucleation, growth and coarsening, as well as for melting and freezing of encapsulated nanoparticles, were integrated into a single model. Although stress and strain effects and the quantum size effect are not included, and the model is limited in the particle sizes it can handle, useful qualitative results are expected. Two additional, related models were also constructed to cover rapid thermal annealing and particle synthesis by repeated injection of monomers.

The pulsed laser melting model and RTA model were used to study the PLM process. The possibility of using PLM and RTA as the quenching and annealing steps in a phase-change memory application was examined; results were inconclusive, as at a reasonable interface energy, the particle size distribution was unstable to the PLM/RTA cycle, but may have been asymptotically approaching a stable distribution beyond the range of the model. The effects of varying laser parameters including the laser fluence, pulse width, and number of repeated pulses were studied; three distinct regimes in terms of the final distribution shape as a function of the laser parameters were identified. The effects of changing the particle concentration were found to be increased laser absorption and increased diffusion with increased concentration. These predictions may be used to tailor future PLM experiments to achieve desirable particle size distributions.

The three models together were used to develop a general theory of particle size distribution narrowing that encompasses laser processing, annealing, colloidal chemistry, and island growth methods. Three effects that produce narrowing were identified: a size-selective transition that creates a significant difference in the solubility of dissolved atoms outside the particle, the geometric effect of growth in volume vs. growth in radius, and the commonly used practice of reporting widths scaled by the average size. These effects are somewhat weak compared to the broadening effect of Ostwald ripening; the critical element of a narrowing scheme is thus suppressing Ostwald ripening, which may be achieved by providing a feedstock of small particles, dissolved atoms, or reactants during growth. No fundamental

limits were found on the monodispersity achievable using such a scheme; widths as narrow as 2% were achieved in the injection simulations, 17% in the simulation of annealing an artificially tailored distribution, and 12% in the PLM simulation.

Bibliography

[1] Y. Wang and N. Herron. "Nanometer-sized semiconductor clusters: materials synthesis, quantum size effects, and photophysical properties". *J. Phys. Chem* **95** (1991), p. 525.

[2] M. Quinten. *Optical Properties of Nanoparticle Systems: Mie and Beyond*. Wiley-VCH Verlag GmbH & Co., 2011.

[3] P. R. Couchman and W. A. Jesser. "Thermodynamic theory of size dependence of melting temperature in metals". *Nature* **269** (1977), p. 481.

[4] Q. Xu et al. "Large melting-point hysteresis of Ge nanocrystals embedded in SiO_2". *Phys. Rev. Lett.* **97** (2006), p. 155701.

[5] C.-W. Yuan et al. "Theory of nanocluster size distributions from ion beam synthesis". *Phys. Rev. Lett.* **102** (2009), p. 146101.

[6] D. O. Yi. "Modeling nucleation, growth and stress: Ge nanocrystals embedded in SiO_2". PhD thesis. University of California, Berkeley, 2005.

[7] D. O. Yi et al. "Modeling nucleation and growth of encapsulated nanocrystals: Kinetic Monte Carlo simulations and rate theory". *Phys. Rev. B* **78** (2008), p. 245415.

[8] X. Peng, J. Wickham, and A. P. Alivisatos. "Kinetics of II-VI and III-V colloidal semiconductor nanocrystal growth: "focusing" of size distributions". *J. Am. Chem. Soc.* **120** (1998), p. 5343.

[9] E. M. Chan et al. "Reproducible, high-throughput synthesis of colloidal nanocrystals for optimization in multidimensional parameter space". *Nano Lett.* **10** (2010), p. 1874.

[10] Y. Yin and A. P. Alivisatos. "Colloidal nanocrystal synthesis and the organic-inorganic interface". *Nature* **437** (2005), p. 664.

[11] S. J. Shin et al. "Embedded binary eutectic alloy nanostructures: a new class of phase change materials". *Nano Lett.* **10** (2010), p. 2794.

[12] S. J. Shin et al. "Structural characterization of GeSn alloy nanocrystals embedded in SiO_2". *Mater. Res. Soc. Symp. Proc.* **1184** (2009), HH04–08.

[13] J. Guzman et al. "Reversible phase changes in Ge-Au nanoparticles". *Appl. Phys. Lett.* **98** (2011), p. 193101.

[14] A. L. Stepanov et al. "Reduction of the size of implanted silver nanoparticles in float glass during excimer laser annealing". *Appl. Surf. Sci.* **136** (1998), p. 298.

[15] A. Takami, H. Kurita, and S. Koda. "Laser-induced size reduction of noble metal particles". *J. Phys. Chem. B* **103** (1999), p. 1126.

[16] S. Inasawa, M. Sugiyama, and Y. Yamaguchi. "Laser-induced shape transformation of gold nanoparticles below the melting point: the effect of surface melting". *J. Phys. Chem.* **109** (2005), p. 3104.

[17] A. K. Jain, V. N. Kulkarni, and D. K. Sood. "Pulsed Laser Heating Calculations Incorporating Vaporization". *Applied Physics* **25** (1981), p. 127.

[18] T. Kim et al. "Heat flow model for pulsed laser melting and rapid solidification of ion implanted GaAs". *J. Appl. Phys.* **108** (2010), p. 013508.

[19] R. F. Wood and G. E. Giles. "Macroscopic theory of pulsed-laser annealing. I. Thermal transport and melting". *Phys. Rev. B* **23** (1981), p. 2923.

[20] J. Trice et al. "Pulsed-laser-induced dewetting in nanoscopic metal films: Theory and experiments". *Phys. Rev. B* **75** (2007), p. 235439.

[21] C.-W. Yuan. "Modeling Size Distribution Evolution of Ion-Beam-Synthesized Nanoclusters in Amorphous Silica". PhD thesis. University of California, Berkeley, 2009.

[22] C.-W. Yuan et al. "Size-distribution evolution of ion-beam-synthesized nanoclusters in silica". *Phys. Rev. B* **80** (2009), p. 134121.

[23] I. D. Sharp et al. "Stable, freestanding Ge nanocrystals". *J. Appl. Phys.* **97** (2005), p. 124316.

[24] I. D. Sharp et al. "Mechanism of stress relaxation in Ge nanocrystals embedded in SiO_2". *Appl. Phys. Lett.* **86** (2005), p. 063107.

[25] G. Mie. "Beiträge zur Optik trüber Median, speziell kolloidaler Metallösungen". *Ann. Phys.* **330** (1908), p. 377.

[26] C. Uhrenfeldt et al. "Near-infrared–ultraviolet absorption cross sections for Ge nanocrystals in SiO_2 thin films: Effects of shape and layer structure". *J. Appl. Phys.* **109** (2011), p. 094314.

[27] L. Viña, S. Logothetidis, and M. Cardona. "Temperature dependence of the dielectric function of germanium". *Phys. Rev. B* **30** (1984), p. 1979.

[28] G.E. Jellison Jr. et al. "Time-resolved reflectivity measurements on silicon and germanium using a pulsed excimer KrF laser heating beam". *Phys. Rev. B* **34** (1986), p. 2407.

[29] Y. M. Niquet et al. "Quantum confinement in germanium nanocrystals". *App. Phys. Lett.* **77** (2000), p. 1182.

[30] C. Bostedt et al. "Strong quantum-confinement effects in the conduction band of germanium nanocrystals". *App. Phys. Lett.* **84** (2004), p. 4056.

[31] S. Sato et al. "Size regulation by bandgap-controlled etching: Application to germanium nanoparticles". *Solid State COmmunications* **149** (2009), p. 862.

[32] C. Bulutay. "Interband, intraband, and excited-state direct photon absorption of silicon and germanium nanocrystals embedded in a wide band-gap lattice". *Phys. Rev. B* **76** (2007), p. 205321.

[33] P. Tognini et al. "Above the band gap structures in Ge nanoparticles: optical-absorption spectra". *Il Nuovo Cimento* **18** (1996), p. 865.

[34] Y.-L. Xu and B. Å .S. Gustafson. "A generalized multiparticle Mie-solution: further experimental verification". *J. Quant. Spectr. & Rad. Trans.* **70** (2001), p. 395.

[35] W. Andrä et al. "Temperature distribution as a function of time around a small spherical heat source of local magnetic hyperthermia". *J. Magn. Magn. Mat.* **194** (1999), p. 197.

[36] H.H. Anderson and E. Johnson. "Structure, morphology and melting hysteresis of ion-implanted nanocrystals". *Nucl. Instr. Meth. Phys. Res. B* **106** (1995), p. 480.

[37] E. Haro-Poniatowski et al. "Melting and solidification of Bi nanoparticles in a germanate glass". *Nanotechnology* **18** (2007), p. 315703.

[38] J.D. McBrayer, R.M. Swanson, and T.W. Sigmon. "Diffusion of metals in silicon dioxide". *J. Electrochem. Soc.: Solid State Science and Technology* **133** (1986), p. 1242.

[39] G. Nesher, L. Kronik, and J. R. Chelikowsky. "*Ab initio* absorption spectra of Ge nanocrystals". *Phys. Rev. B* **71** (2005), p. 035344.

[40] H.-Ch. Weissker, J. Furthmüller, and F. Bechstedt. "Optical properties of Ge and Si nanocrystallites from *ab initio* calculations: I. Embedded nanocrystallites". *Phys. Rev. B* **65** (2002), p. 155327.

[41] H.-Ch. Weissker, J. Furthmüller, and F. Bechstedt. "Optical properties of Ge and Si nanocrystallites from *ab initio* calculations: II. Hydrogrenated nanocrystallites". *Phys. Rev. B* **65** (2002), p. 155328.

[42] D. V. Melnikov and J. R. Chelikowsky. "Absorption spectra of germanium nanocrystals". *Sol. State Comm.* **127** (2003), p. 361.

[43] B. N. Chichkov et al. "Femtosecond, picosecond and nanosecond laser ablation of solids". *Appl. Phys. A* **63** (1996), p. 109.

[44] V. M. Glazov and O. D. Shchelikov. "Volume changes during melting and heating of silicon and germanium melts". *High Temperature* **38** (2000), p. 405.

[45] Z. Jian et al. "Solid-liquid interface energy of silicon". *Acta Materialia* **54** (2006), p. 3227.

[46] C. N. Boswell-Koller. "Theoretical Investigation of Binary Eutectic Alloy Nanoscale Phase Diagrams". PhD thesis. University of California, Berkeley, 2012.

[47] I. M. Lifshitz and V. V. Slyozov. "The Kinetics of Precipitation from Supersaturated Solutions". *J. Phys. Chem. Solids* **19** (1961), p. 35.

[48] Z. Fang, B. R. Patterson, and M. E. Turner. "Influence of Particle Size Distribution on Coarsening". *Acta Metall. Mater.* **40** (1992), p. 713.

[49] F. M. Ross, J. Tersoff, and R. M. Tromp. "Coarsening of self-assembled Ge quantum dots on Si(001)". *Phys. Rev. Lett.* **80** (1998), p. 984.